Electronic Supplementary Material (ESI) for Physical Chemistry Chemical Physics.

Supplementary Information

BCC-Cu Nanoparticles: From a Transient to a Stable Allotrope by Tuning Size and Reaction Conditions

Jan L. Alfke[a,b]†, Andreas Müller[a] †, Adam H. Clark[b], Antonio Cervellino[b], Milivoj Plodinec, Aleix Comas-Vives[c,d], Christophe Copéret[a,*], and Olga V. Safonova[b,*]

[a.] *Department of Chemistry and Applied Biosciences, ETH Zurich, Vladimir Prelog Weg 2, Zurich, Switzerland*
[b.] *Paul Scherrer Institute, Forschungsstrasse 111 CH-5232 Villigen, Switzerland*
[c.] *Institute of Materials Chemistry, TU Wien, 1060 Vienna, Austria.*
[d.] *Departament de Química, Universitat Autònoma de Barcelona, 08193, Cerdanyola del Vallès, Catalonia, Spain.*
[e.]
[f.] *† Shared first authorship*

Table of Contents

1: Synthesis of Materials

General considerations:

Unless otherwise indicated, all experiments were undertaken using conventional air-free techniques under Ar: glove box or Schlenk techniques. Benzene (C_6H_6) was distilled from purple Na^0/benzophenone under Ar and stored over activated molecular sieves (4 Å, Merck). $[Mg(CH_2Ph)_2(THF)_2]$, $Cu_4O^tBu_4$ and $[Cu_5Mes_5]$ were synthesized as described in earlier literature[1,2,3]. Molecular Sieves (4 Å, Merck) were activated under high vacuum (10^{-5} mbar) overnight at 350 ^oC. Elemental analysis was performed by Mikroanalytisches Labor Pascher. An der Pulvermühle 1. D - 53424 Remagen-Bandorf. For analysis of trace metals (Cu) ICP-AES was used.

Synthesis of $SiO_{2\text{-}500}$

Silica (Aerosil Degussa, 200 $m^2\ g^{-1}$) was compacted with deionized water, dried at 100°C for 7 days, crushed and sieved (250−400 µm) for easier handling. $SiO_{2\text{-}500}$ was calcined at 500 °C in air for 4 hours (ramp: 5 °C min^{-1}), cooled to room temperature and then treated under high vacuum (10^{-5}mbar) at 500°C for 12 hours. Quantification of the -OH density of supports using $[Mg(CH_2Ph)_2(THF)_2]$ yielded a concentration of 0.54 mmol/g for $SiO_{2\text{-}500}$.

Synthesis of $[Cu^I]@SiO_2$

To a suspension of $SiO_{2\text{-}500}$ (1.0 g, 0.5 mmol SiOH) in 2 mL of benzene, a solution of $[Cu_4O^tBu_4]$(0.11g, 0.2mmol) in 5 mL of benzene was added slowly. The mixture was stirred for 4 hours, limiting the stirring rate to 100 rpm in order to avoid breaking up the silica agglomerates. Afterwards, the solvent was remove by filtration, and the remaining white solid was washed three times with 5 mL of benzene each. Afterwards, the solid was dried under high vacuum (10^{-5} mbar).

Synthesis of CuNP@SiO_2

1g of [Cu^I]@SiO_2 was placed under a flow of H_2 and heated to 500 ^oC for 4 hours, with a ramp rate of 5 ^oC /min. After cooling down to room temperature, the resulting red-brown solid was evacuated again under high vacuum (10^{-5} mbar).

Synthesis of [Cu^I-Mes]@SiO_2

[Cu_5Mes_5] was synthesized according to literature procedures[3].

A solution of [Cu_5Mes_5](0.157.6g, 0.2mmol) in 5 mL of benzene was added slowly to a suspension of $SiO_{2\text{-}500}$ (1.0 g, 0.5 mmol SiOH) in 2 mL of benzene,. The mixture was stirred for 4 hours at the stirring rate below 100 rpm to avoid breaking up the silica agglomerates. Afterwards, the solvent was removed by filtration; and the remaining white solid was washed three times, each one with 5 mL of benzene. Afterwards, the solid was dried under high vacuum (10^{-5} mbar).

2: Transmission Electron Microscopy (TEM)

General considerations:

Transmission electron microscopy (TEM) was measured on a JEOL JEM-1400 Plus microscope. For the determination of the particle size distribution, >200 individual particles were considered, and the mean particle size and standard deviation are given according to a normal distribution function. Powdered samples in solid form were applied to a Lacy-C 300 mesh Cu grid (Ted Pella). Samples were exposed to air prior to measurement.

TEM images FCC

CuNP@SiO_2

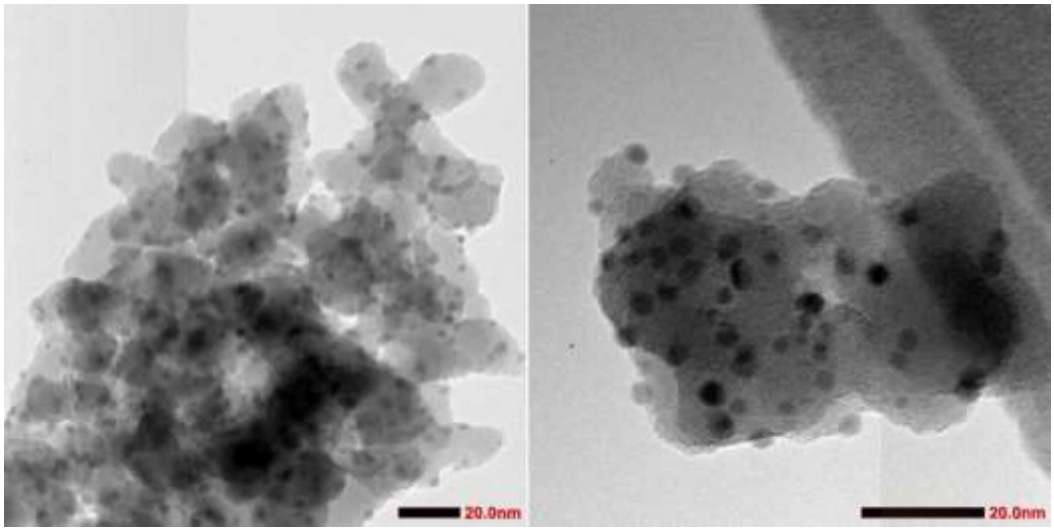

Figure S1: Representative TEM images of FCC CuNP@SiO_2

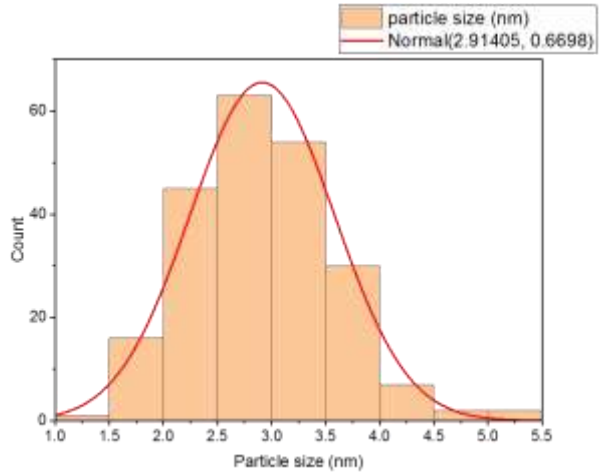

Figure S2: Particle size distribution of FCC CuNP@SiO_2

BCC CuNP@SiO_2

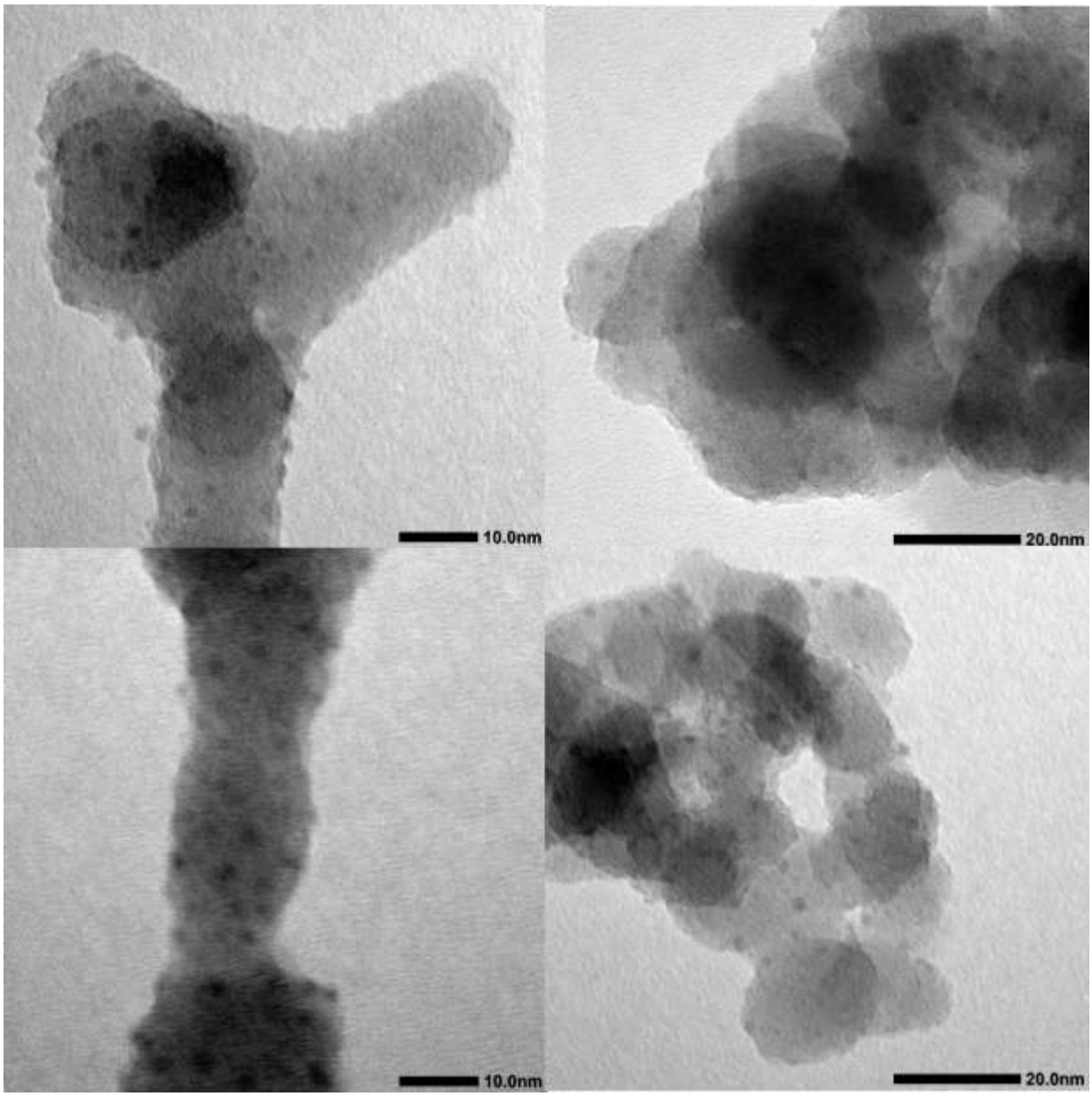

Figure S3: Additional TEM images of BCC Cu-SiO_2

2.1 High Resolution TEM

High-resolution transmission electron microscopy (HRTEM) was performed using a double corrected JEOL JEM-ARM300F Grand ARM "Vortex" operated at 300 kV, equipped with a fast GATAN OneView camera 4Kx4K.

Both samples were prepared inside the glovebox by dry casting on a TEM Nickel grid covered with lacey carbon. To avoid oxidation of Cu nanoparticles, samples were transferred to the microscope in air-free conditions by vacuum transfer TEM holder.

FCC Cu-SiO_2

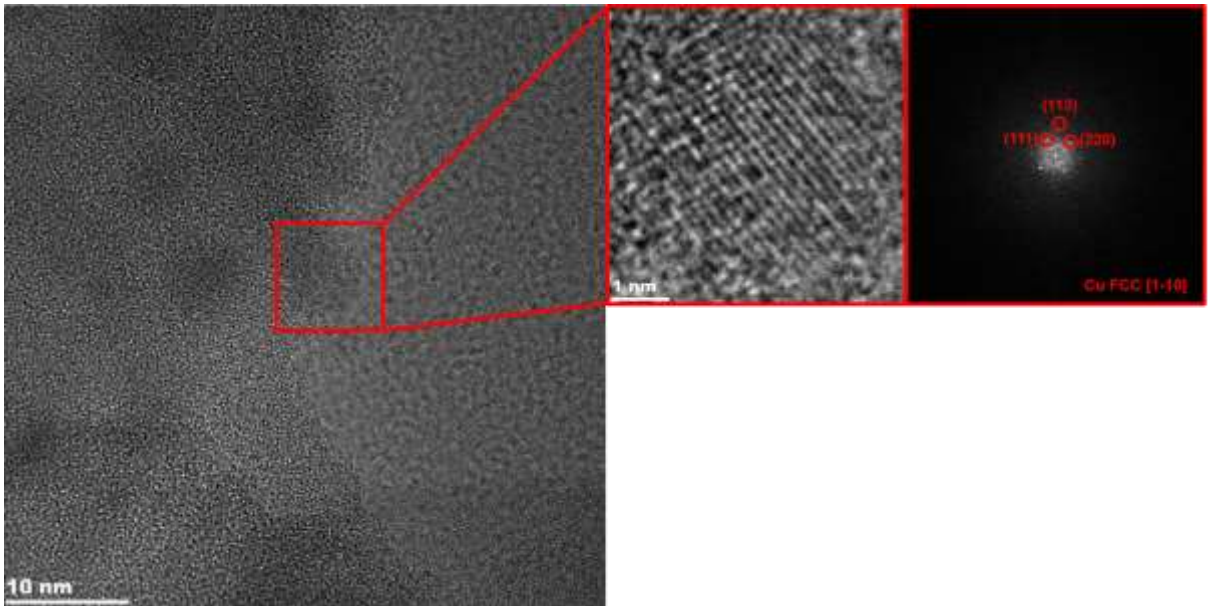

Figure S4: Representative High resolution TEM images of FCC Cu-SiO_2

BCC Cu-SiO_2

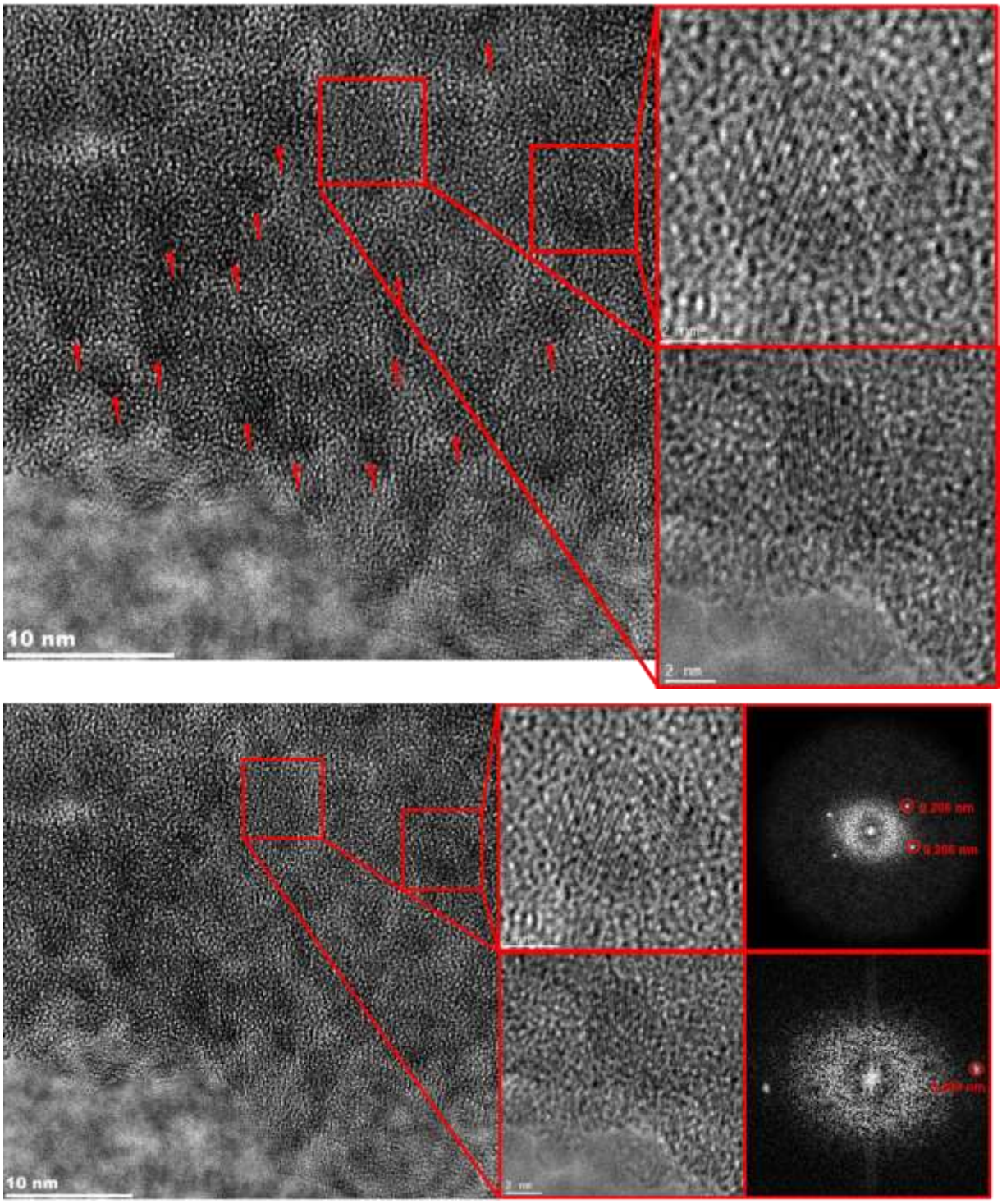

Figure S5: Representative High resolution TEM image of BCC Cu-SiO_2

3: X-Ray Absorption Spectroscopy (XAS)

General considerations:

XAS measurements were carried out at the Cu K edge at the SuperXAS beamline at SLS (PSI, Villigen, Switzerland)[3]. The storage ring was operated at 2.4 GeV in top-up mode with a ring current of around 400 mA. The incident photon beam provided by a 2.9 T super bend magnet source was selected by a water or liquid nitrogen cooled Si (111) quick-EXAFS monochromator and the rejection of higher harmonics and focusing were achieved by a rhodium- or silicon- coated collimating mirror at 2.5 mrad. Acquisition time for each spectrum was 0.01 or 0.5s. After focusing with rhodium-coated toroidal mirror, the beam size on the sample was 500 x 100 μm. During measurement, the quick XAS monochromator was rotating with 1 Hz frequency in 1.5-2 deg angular range and X-ray absorption spectra were collected in transmission mode using ionization chambers specially developed for quick data collection with 2 MHz frequency[4]. The beamline energy was calibrated with a Cu reference foil to the Cu K edge position at 8979.0 eV.

For *in situ* experiments, 20 mg of **[Cu^{I}]@SiO_2** were loaded into a 3mm outside diameter quartz glass capillary with a wall thickness of 0.2mm in an Ar sealed glovebox. The capillary was equipped with a bypass to allow replacing all air in the lines with Ar prior to measurement. Gas flows were controlled with Bronkhorst mass flow controllers. Gas switches were done using a VALCO VICI millisecond switch valve. H_2 (99.9999%) and Ar(99.9999%) were supplied by PanGas. 10%H_2 in Ar was obtained by mixing pure Ar and H_2 with two different mass flow controllers. Samples were heated using a custom-built infrared heater (Elstein-Werk M. Steinmetz GmbH & Co. KG (Germany), 30 mm length, with two heating elements – one above and one below sample capillary). Temperature calibration was performed in the range between 25-510^{o}C.

Data processing was done by standard procedures using the ProQEXAFS[5] software for calibration, interpolation, normalisation and data averaging. Further analysis of the EXAFS was performed using the Demeter software package[6]. The amplitude

reduction factor was obtained by fitting a Cu foil reference for the Cu K-edge and was refined as 0.88.

XAS TPR reduction of [Cu^{I}]@SiO_2

In a first step, the sample was measured at room temperature under static Ar for 10 minutes in order to obtain high quality EXAFS. Afterwards, the sample was placed under a flow of H_2 (10mL/min) and heated to 500^{o}C at a ramp rate of 5^{o}C/min. After 500^{o}C was reached, the sample was allowed to cool to room temperature and measured again for 10 minutes. XAS was continuously measured during all heating ramps and plateaus.

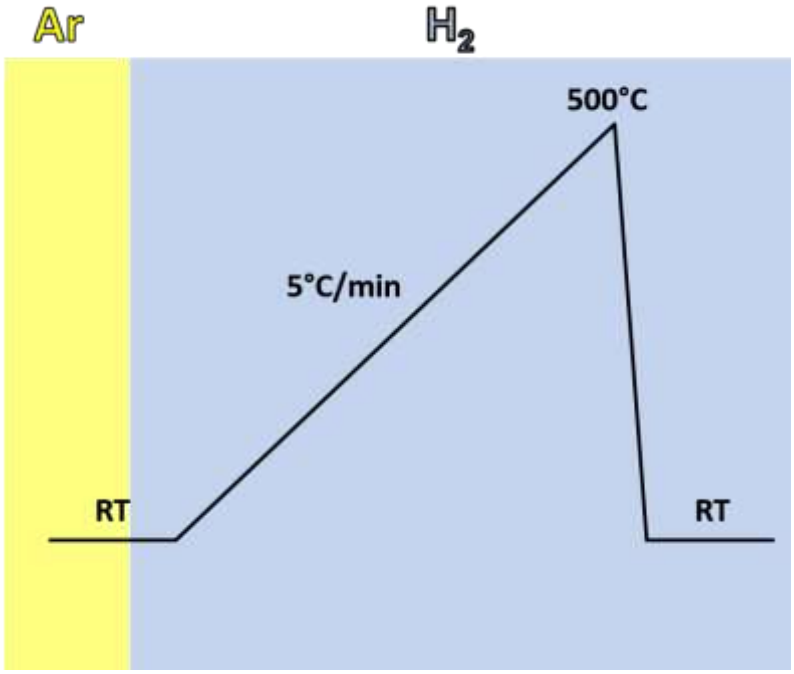

Figure S6: Experimental protocol of the in situ H_2-TPR XAS experiment

Reduction of [Cu^{I}]@SiO_2 at low temperature and stability test in Ar

In a first step, the sample was measured at room temperature under Ar for 10 minutes in order to obtain high quality EXAFS. Afterwards, the sample was placed under a flow of H_2 (10 mL/min) and heated to a temperature of 110 ^{o}C at a ramp rate of 5 ^{o}C/min. After 30 minutes at 110 ^{o}C, the gas flow was switched to Ar (10mL/min), and held at 100 ^{o}C for another 30 minutes. The sample was then cooled back down to room temperature at a ramp rate of 10 ^{o}C/min, and XAS was acquired for another 10

minutes. Afterwards, the sample, still under a flow of Ar, was heated to 500 ^{o}C at a ramp rate of 5 ^{o}C/min. After reaching 500 ^{o}C, the sample was allowed to cool back to room temperature. After reaching it, XAS was acquired for another 10 minutes. XAS was continuously measured during all heating ramps and plateaus.

Reduction of [Cu^{I}]@SiO_2 under 10%H_2

In a first step, the sample was measured at room temperature under static Ar for 10 minutes in order to obtain high quality EXAFS. Afterwards, the sample was placed under a flow of H_2 (1mL/min) and Ar (9 mL/min) and heated to 500 ^{o}C at a ramp rate of 5 ^{o}C/min. After reaching 500 ^{o}C, it was held at that point for 2 hours. After allowing the sample to cool down to room temperature, XAS was again acquired for 10 minutes. XAS was continuously measured during all heating ramps and plateaus.

After the experiment was completed, the sample was exposed to air and recovered for TEM measurements.

In situ reduction of [Cu^{I}-Mes]@SiO_2 under 100% H_2

In a first step, the XAS of the sample was measured at room temperature under static Ar flow for 10 minutes, to obtain high quality EXAFS. Afterwards, the sample was placed under a flow of H_2 (10 mL/min) and heated to 500 ^{o}C at a ramp rate of 5 ^{o}C/min. After reaching 500 ^{o}C, it was dwelled for 2 hours. After cooling to room temperature, XAS was again acquired for 10 minutes.

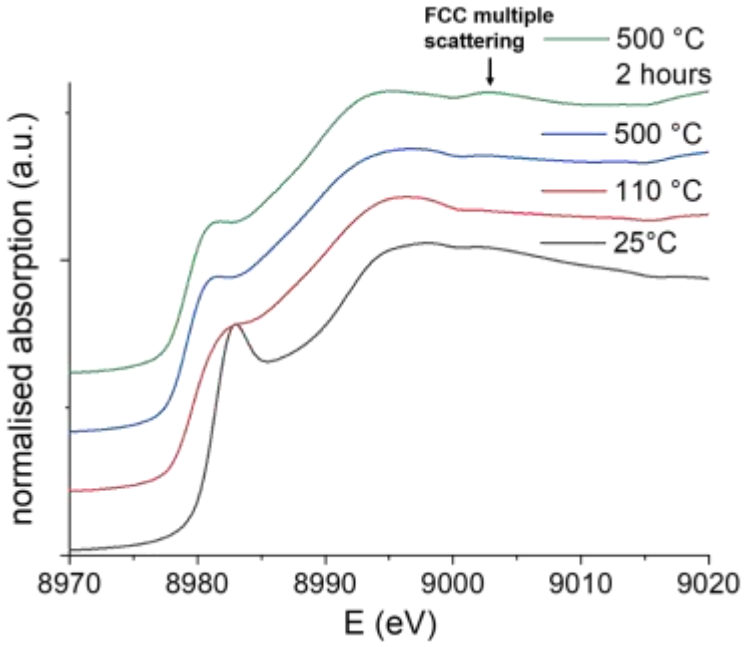

*Figure S7: Cu K-edge XANES of **[Cu^{I}-Mes]@SiO$_2$** during H_2-TPR at 25 °C, 110°C, 500 °C and at 500 °C after 2 hours. The FCC-related multiple scattering feature (**C**) begins to emerge at 500 °C and intensifies after 2 hours.*

Multivariate Curve resolution (MCR)

MCR analysis was carried out using the ProQEXAFS[5] software. In total, 8089 spectra were recorded during the experiment, which were averaged by 80, normalised and then cropped to only include the XANES region between 8970-9020 eV. Initial guesses for the pure spectral components were obtained using the SIMPLISMA[7] algorithm, a pure variable selection method. These initial guesses were then refined via MCR using proQEXAFS. Non-negativity and closure-to-1 constraints were imposed on the concentrations of the spectral components. SVD analysis (Figure S7) carried out with proQEXAFS shows a significant increase in explained variance between 2 and 3 component, and a smaller increase from 3 to 4 components, meaning that 3 components are needed at least (additionally reflected in the reducing decrease in the component eigenvalues with the addition of more components). To decide between a 3 or 4 component model, MCR analysis was carried out with both 3 and 4 components, and the results examined more closely.

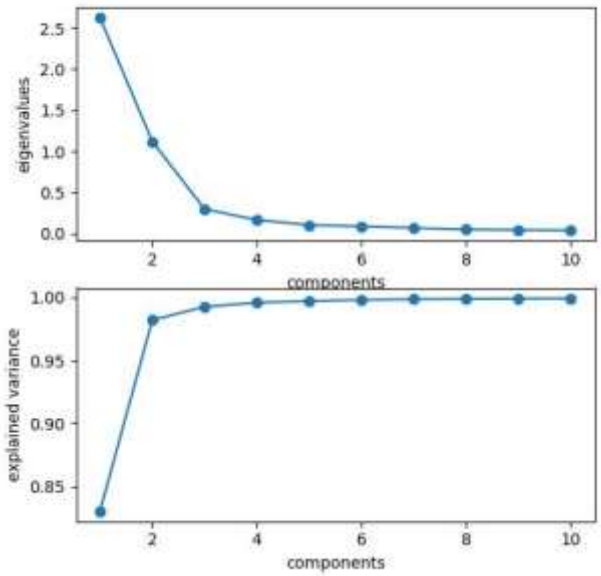

Figure S8: SVD analysis of the in situ H_2-TPR data

In the three component model, the components are the initial and final state, as well as an intermediate component (Fig. S8). The component peaks and decays at the same points as **Int 2** in the four component model, but appears slightly earlier. At around 110°C, where in the four component model **Int1** was dominant, there is also a significant contribution of the final state component. Comparing the fits of both models in the region where **Int1** is at its highest concentration, reveals that the four component model describes the data significantly better here, as can be seen by visual inspection of the fit or in the fit residuals (Fig. S10). The fit of the 3 component model is especially poor at the shoulder feature **A** and at the white line, the regions of the spectrum which contain structural information. In the regions where the other components are dominant, the two models are of comparable quality, as seen again by the fit residuals (Fig. S 9-12). Therefore, the 4 component is deemed to be the best description of the dataset. The lack of fit (LOF) (Fig. S 13) also shows that the model chosen describes the entire dataset well, and not only the points which were discussed here.

Additionally, the 4 component model is also more plausible from a chemical perspective. While it makes sense that small clusters are formed first and then grow, it is hard to justify why the final state should be formed first, then be converted into an intermediate, only to be reformed later.

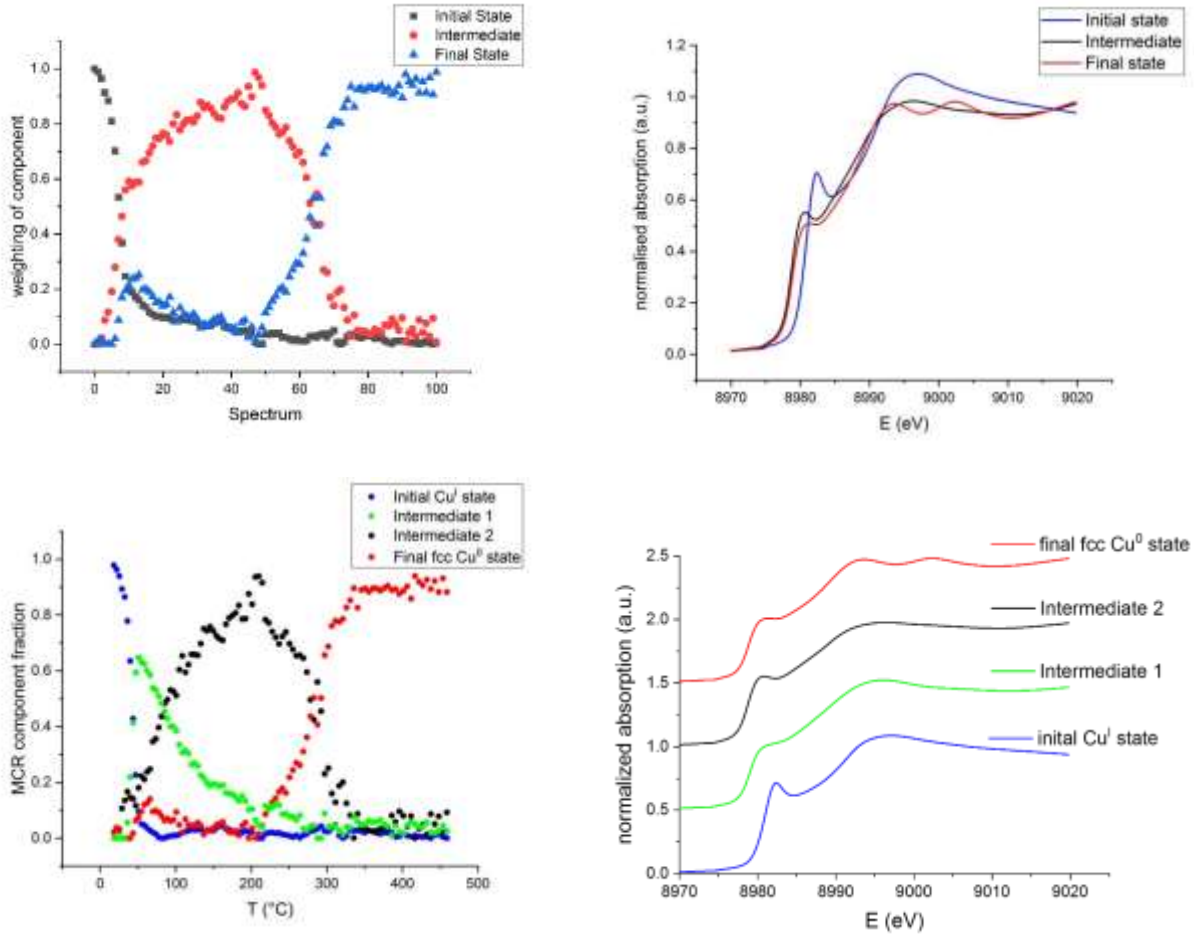

*Figure S9: Multivariate curve resolution analysis of the in situ H_2 TPR reduction of **[Cu^{I}]@SiO$_2$.** Left: Weighting of components. Right: Spectrally pure components. Top: 3 component model. Bottom: 4 component model.*

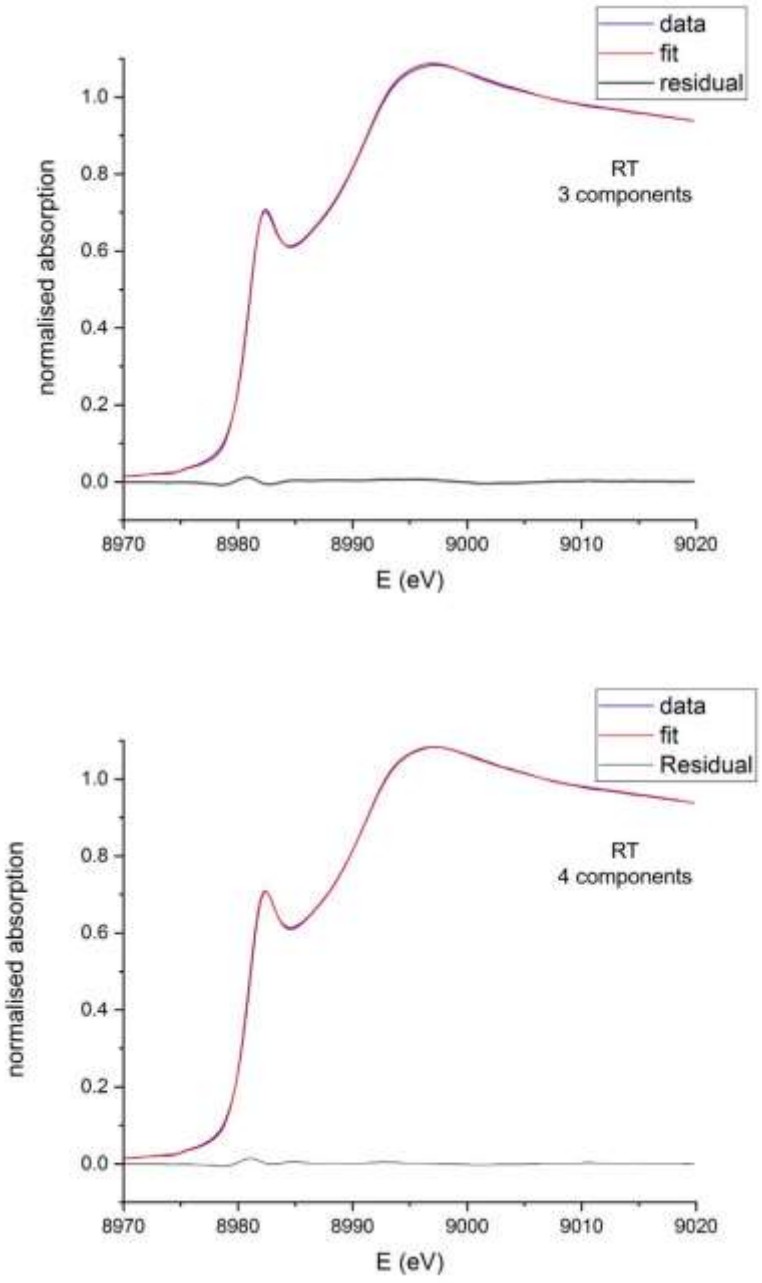

Figure S10: MCR Fit(blue) to the data(orange) at the beginning of the experiment using three components (Top), and four components (bottom)

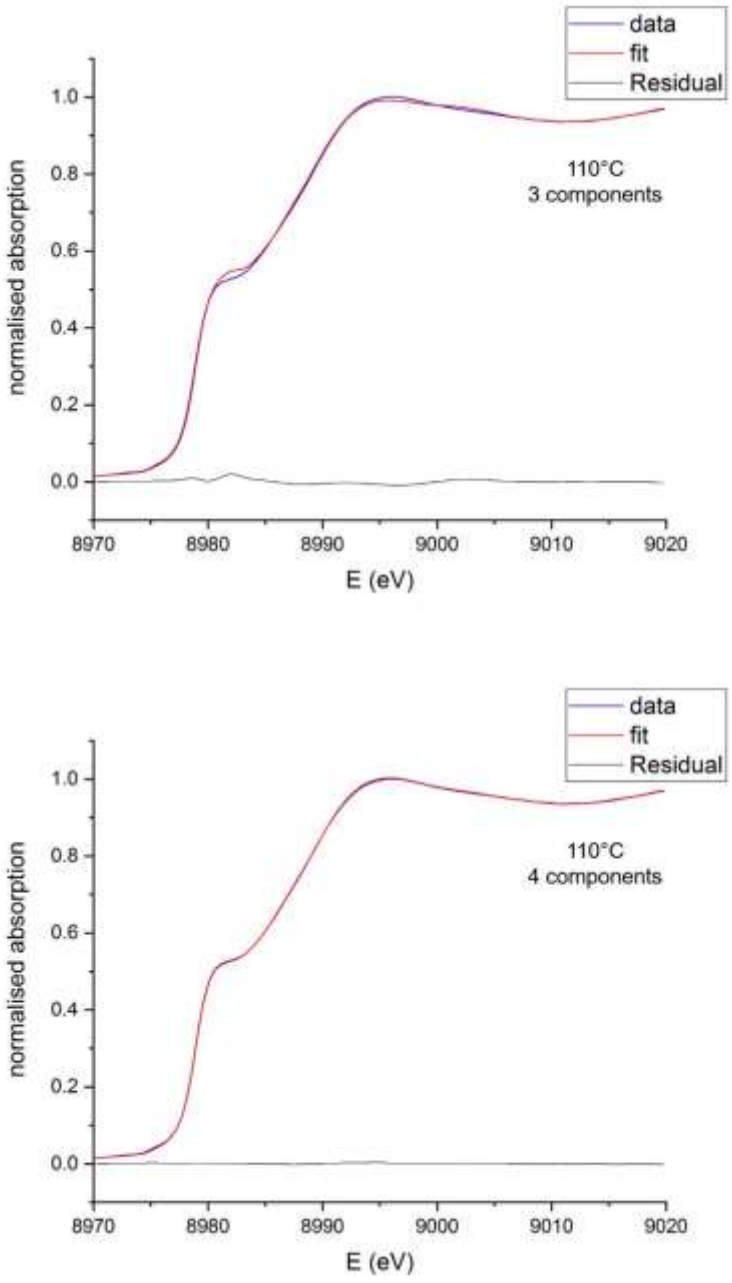

Figure S11: MCR Fit(blue) to the data(orange) at the 13th spectrum at 110°C, where the first intermediate component is most pronounced, using three components (Top), and four components (bottom)

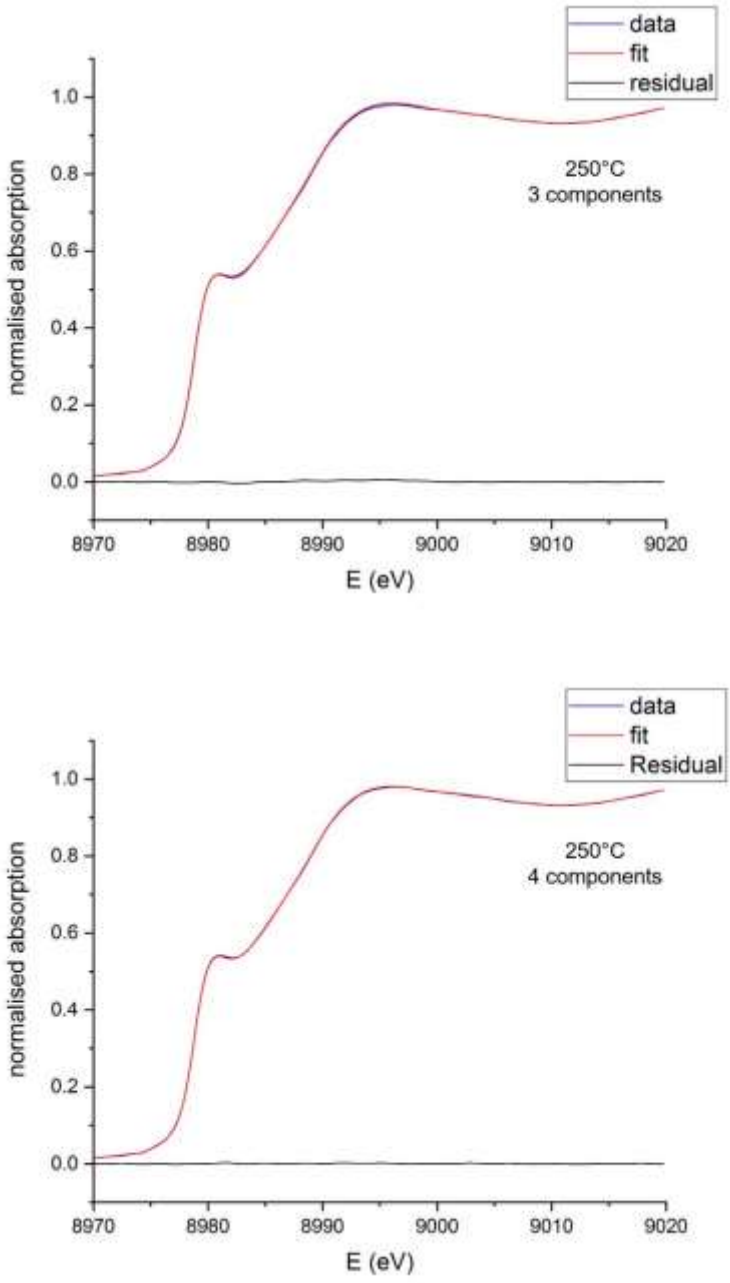

Figure S12: MCR Fit to the data at the 50th spectrum at 250°C, where the second intermediate component is most pronounced, using three components (Top), and four components (bottom)

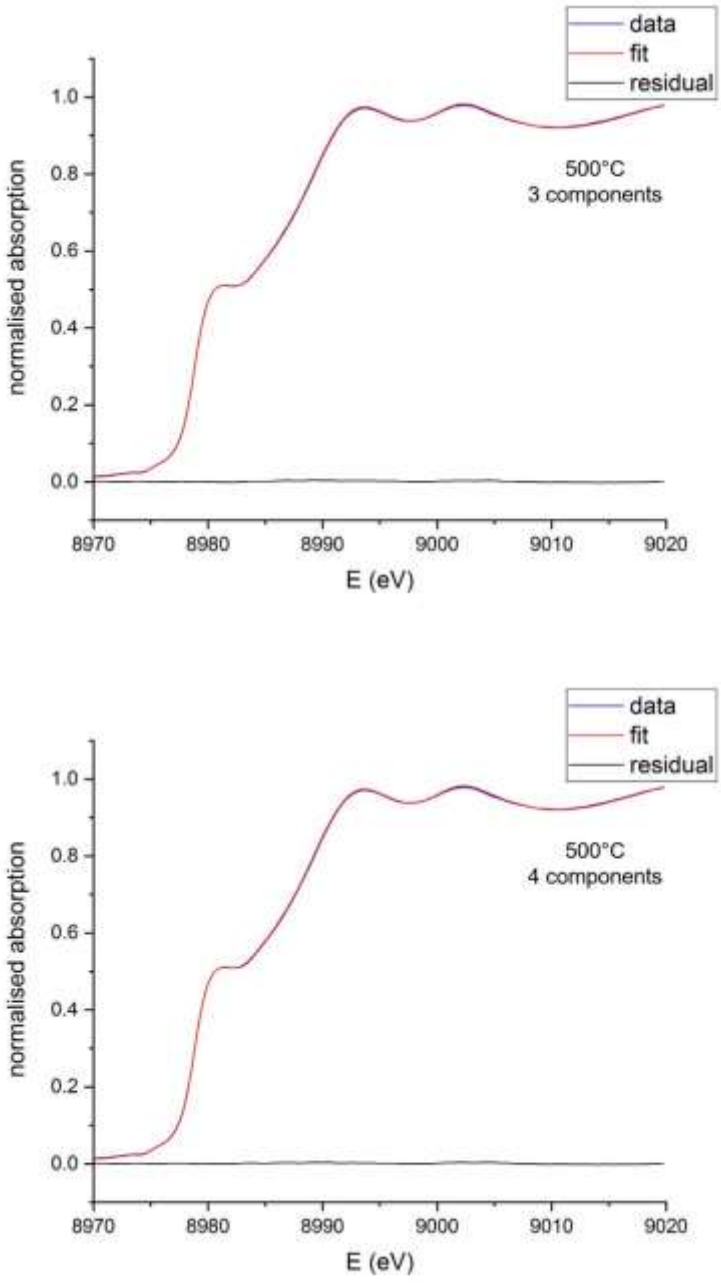

Figure S13: MCR Fit to the data at the final spectrum at 500°C, where the second intermediate component is most pronounced, using three components (Top), and four components (bottom)

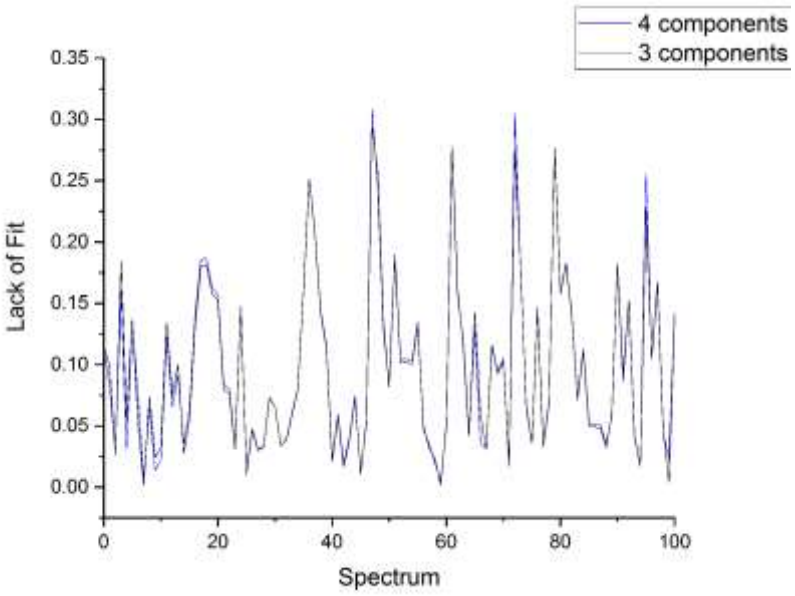

Figure S14: Lack of fit throughout the entire datarange for both the 3 and 4 component models

EXAFS fits

The Fourier transform for the EXAFS fits was carried out with a k-weighting of 2, in a k-range of 3-11, using a Hanning window with dk=1. The chosen R range for the fits was 1-3 with a Hanning window with dR=0.5.

S_0^2 determination with Cu foil

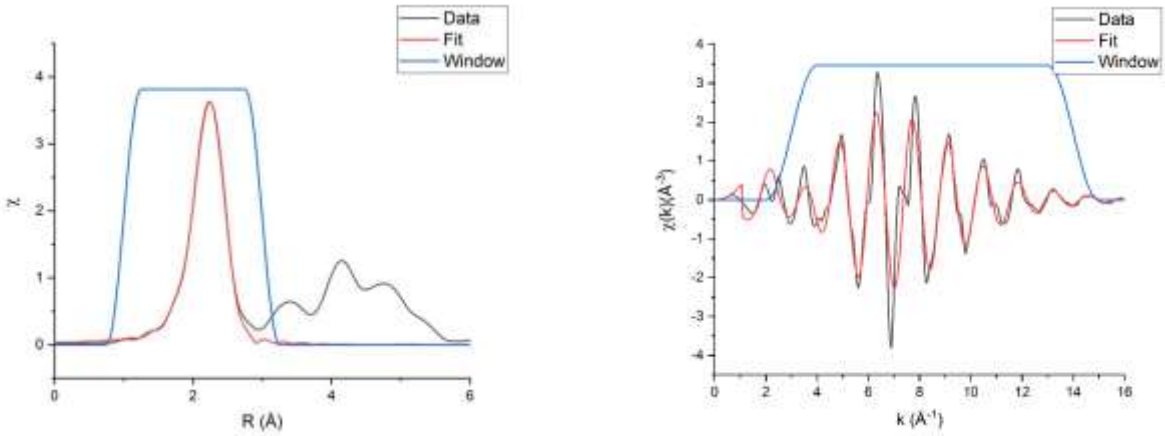

Figure S15: Cu K-edge EXAFS of Cu foil in R and k space, including fit

Table ST1: Cu K-edge EXAFS fitting parameters for Cu foi

Path	$N*S_0^2$	R(Å)	$\sigma^2(Å^2)$	E_0(eV)
Cu-Cu	12*0.88 ± 0.04	2.542 ± 0.003	0.009 ±0.0003	4.5 ± 0.4

[Cu^I]@SiO$_2$

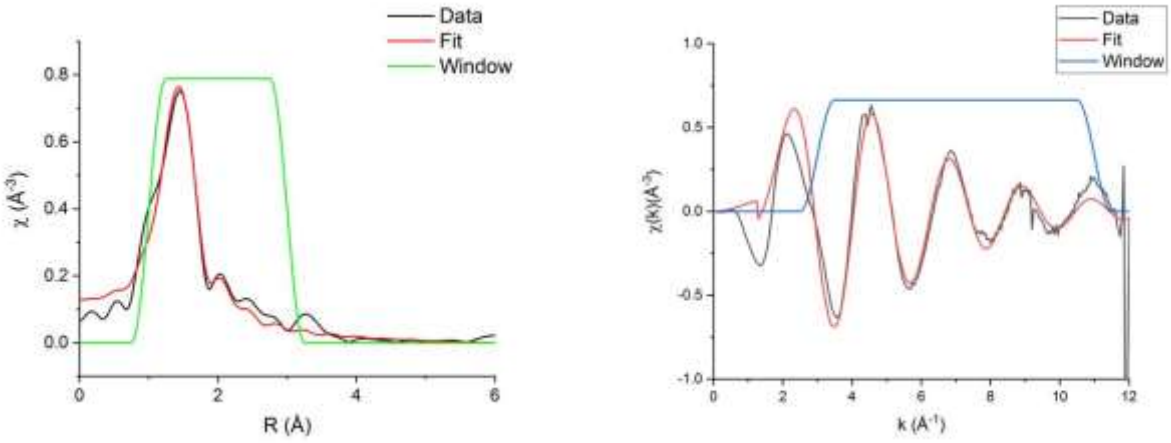

Figure S16: Cu K-edge EXAFS of [Cu^I]@SiO$_2$ in k and R space, including fit.

Table ST2: Cu K-edge EXAFS fitting parameters for [Cu^I]@SiO$_2$

Path	N	R(Å)	$\sigma^2(Å^2)$	E_0(eV)
Cu-O	1.7 ± 0.2	1.86 ±0.01	0.005 ± 0.002	7 ± 2

In situ fits during H_2 TPR

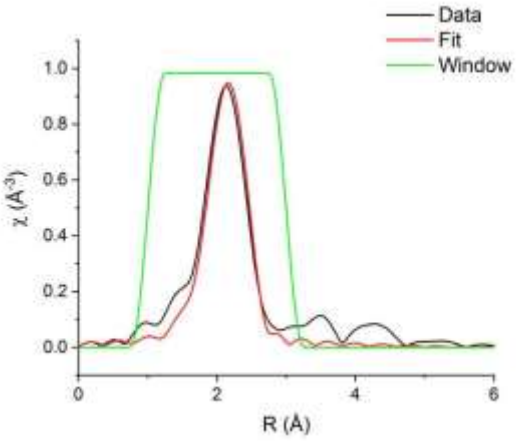

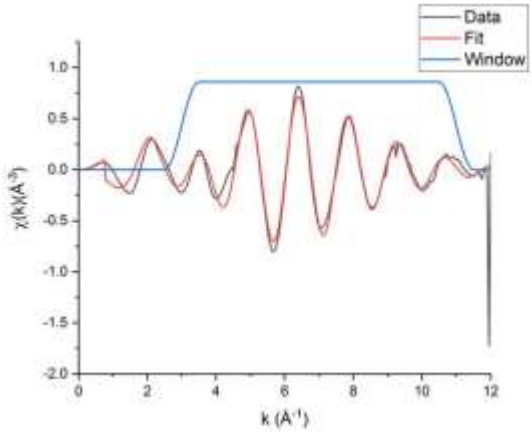

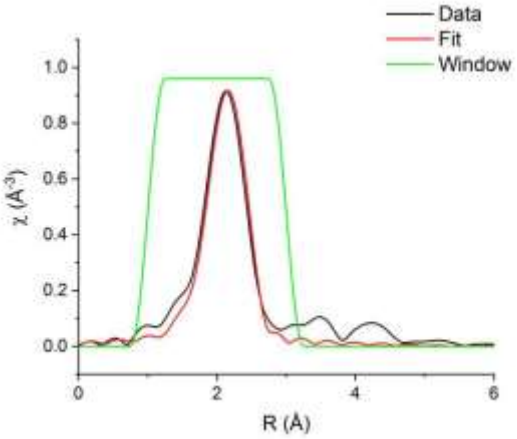

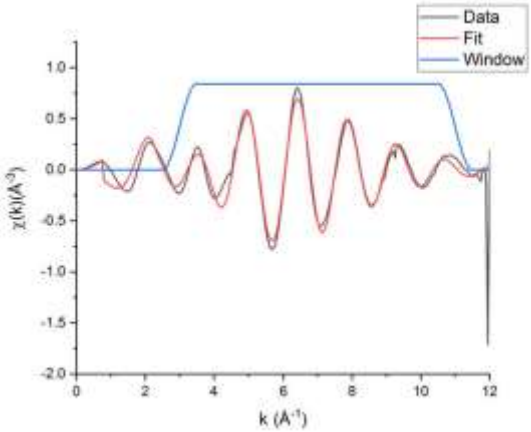

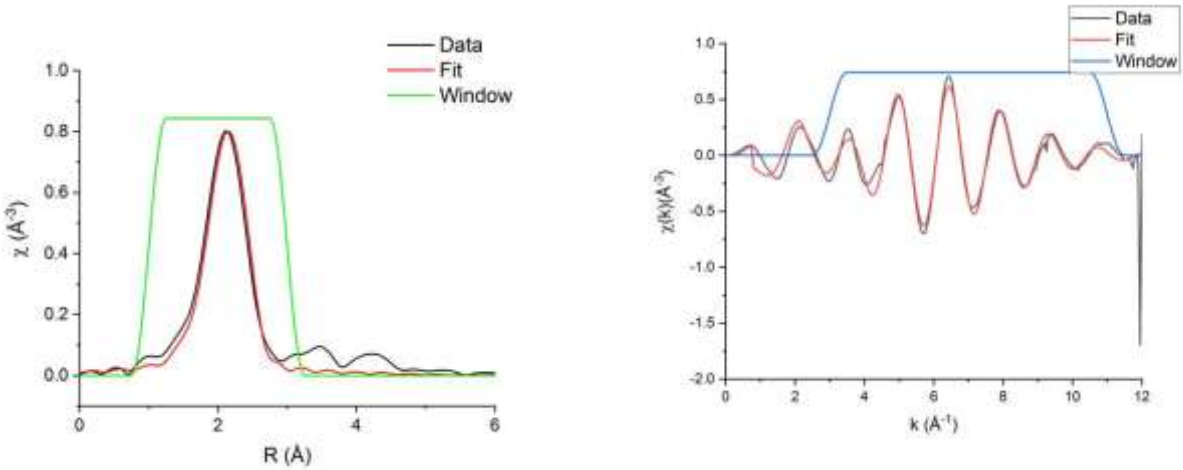

Figure S17: Cu K-edge EXAFS of [Cu^{I}]@SiO_2 during H_2 TPR in k and R space at (from top to bottom) 110^{o}C, 160^{o}C and 210^{o}C, including fit.

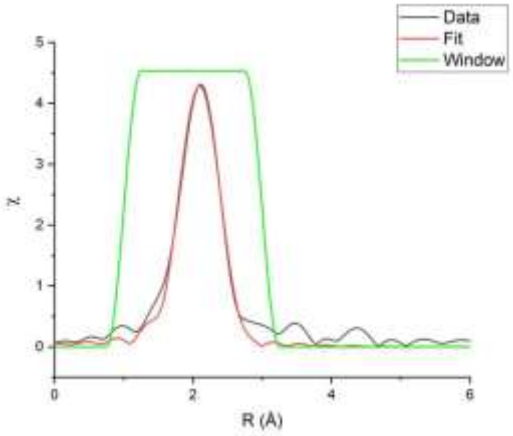
Data
Fit
Window
χ
R (Å)

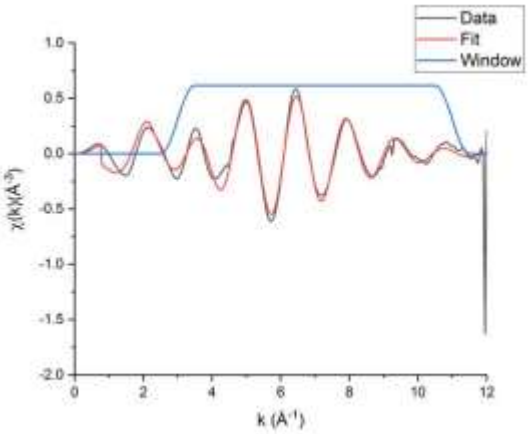
Data
Fit
Window
χ(k)(Å⁻³)
k (Å⁻¹)

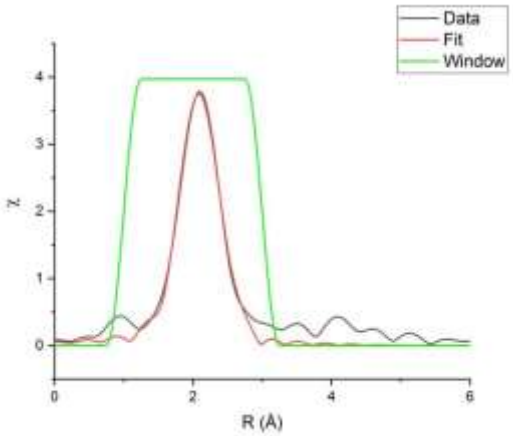
Data
Fit
Window
χ
R (Å)

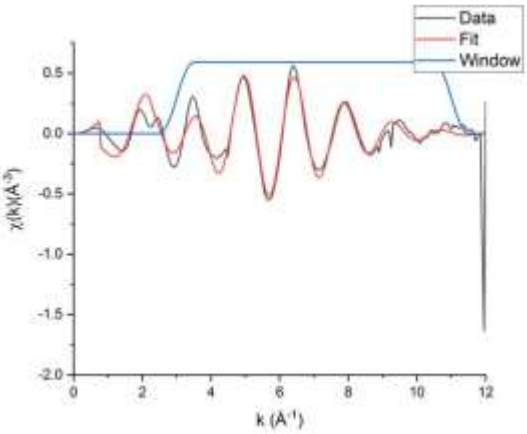
Data
Fit
Window
χ(k)(Å⁻³)
k (Å⁻¹)

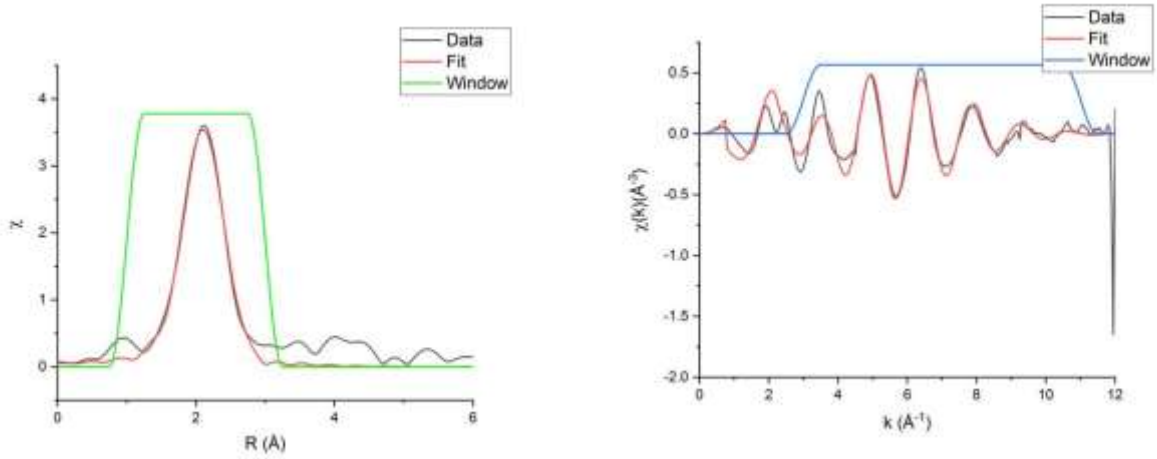

Figure S18: Cu K-edge EXAFS of [Cu^{I}]@SiO_2 during H_2 TPR in k and R space at (from top to bottom) 270°C, 350°C and 400°C, including fit.

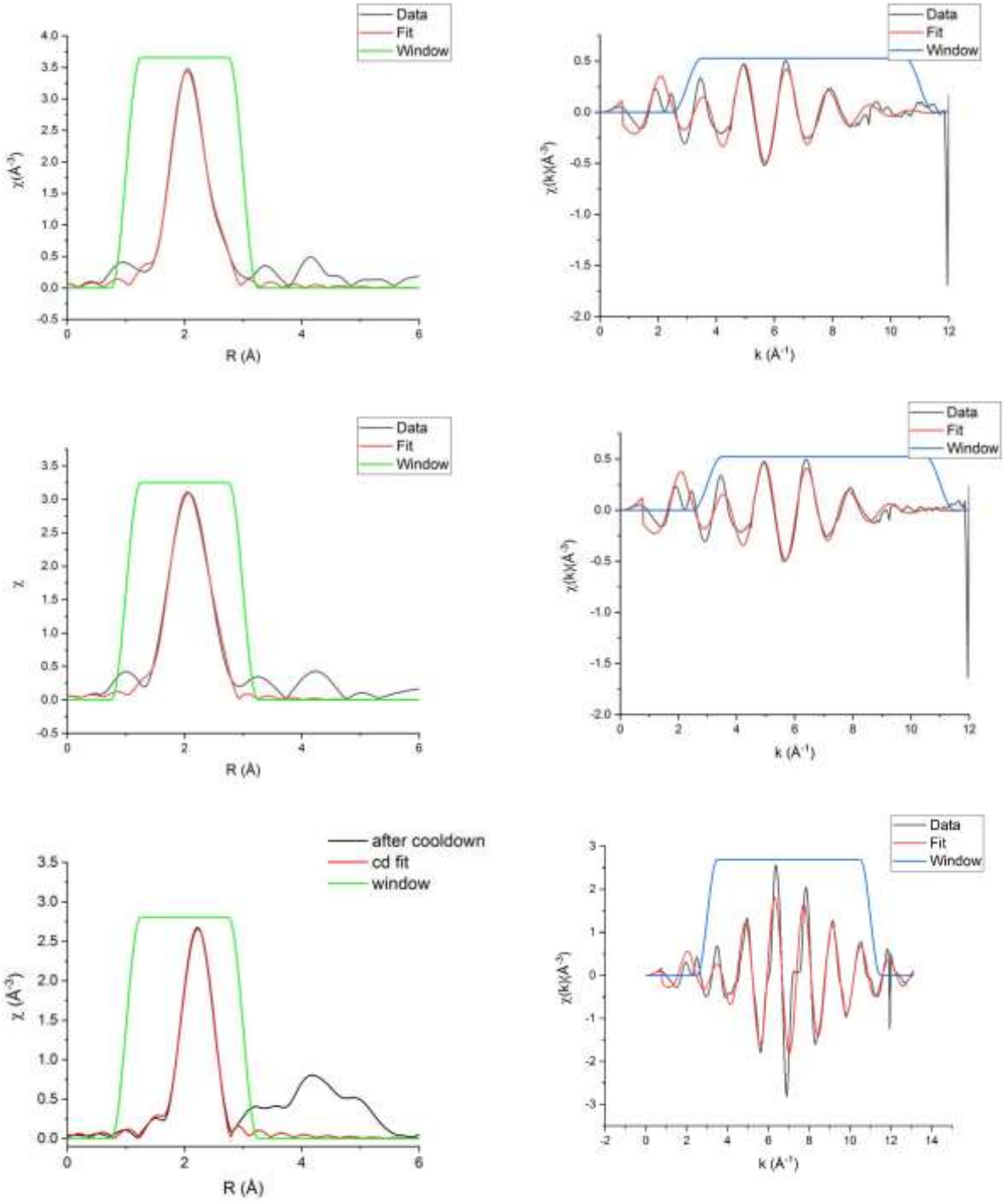

Figure S19: Cu K-edge EXAFS of [Cu^{I}]@SiO_2 during H_2 TPR in k and R space at (from top to bottom) 450°C, 500°C and after cool down at room temperature, including fit.

4: Synchrotron powder X-Ray Diffraction (pXRD)

General Considerations:

Synchrotron based pXRD was measured at the X04SA-MS beamline at the Swiss Light Source (SLS). The beam energy was at 21.8 kEV, and the wave length was determined precisely to be 0.56872(6) Å using a SiO_2 powder standard. X-ray intensity was measured using the MYTHEN II detector[8]. Theoretical diffraction patterns for BCC and FCC structured Cu were calculated from the DFT optimized structures using VESTA[7]. Samples were heated using the custom-built infrared heater (Elstein-Werk M. Steinmetz GmbH & Co. KG (Germany), 30 mm length, with two heating elements – one above and one below sample capillary), which was also used for the XAS measurements. Temperature calibration was performed in the range of 25-510^{o}C.

Synchrotron pXRD TPR of [Cu^{I}]@SiO_2

The sample was packed inside a 1mm quartz glass capillary, equipped with a bypass to allow air free loading. The sample was then placed under a flow of H_2 (5mL/min). After measuring the diffraction pattern at room temperature for 30 minutes, the sample was successively heated to 110 ^{o}C, 150 ^{o}C, 200 ^{o}C, 300 ^{o}C, 400 ^{o}C and 500 ^{o}C at a ramp rate of 10^{o}C/min. At each target temperature, the diffraction pattern was measured for 30 minutes. At 500 ^{o}C, the pattern was acquired for 2 hours. The entire diffraction patterns are shown in Figure S 11. Crystallite sizes were estimated by fitting the diffraction peak with a Gaussian model, and then calculating the size with the Scherrer equation, assuming a Scherrer shape factor of 0.9. Fits are given in Figures S12 and S13.

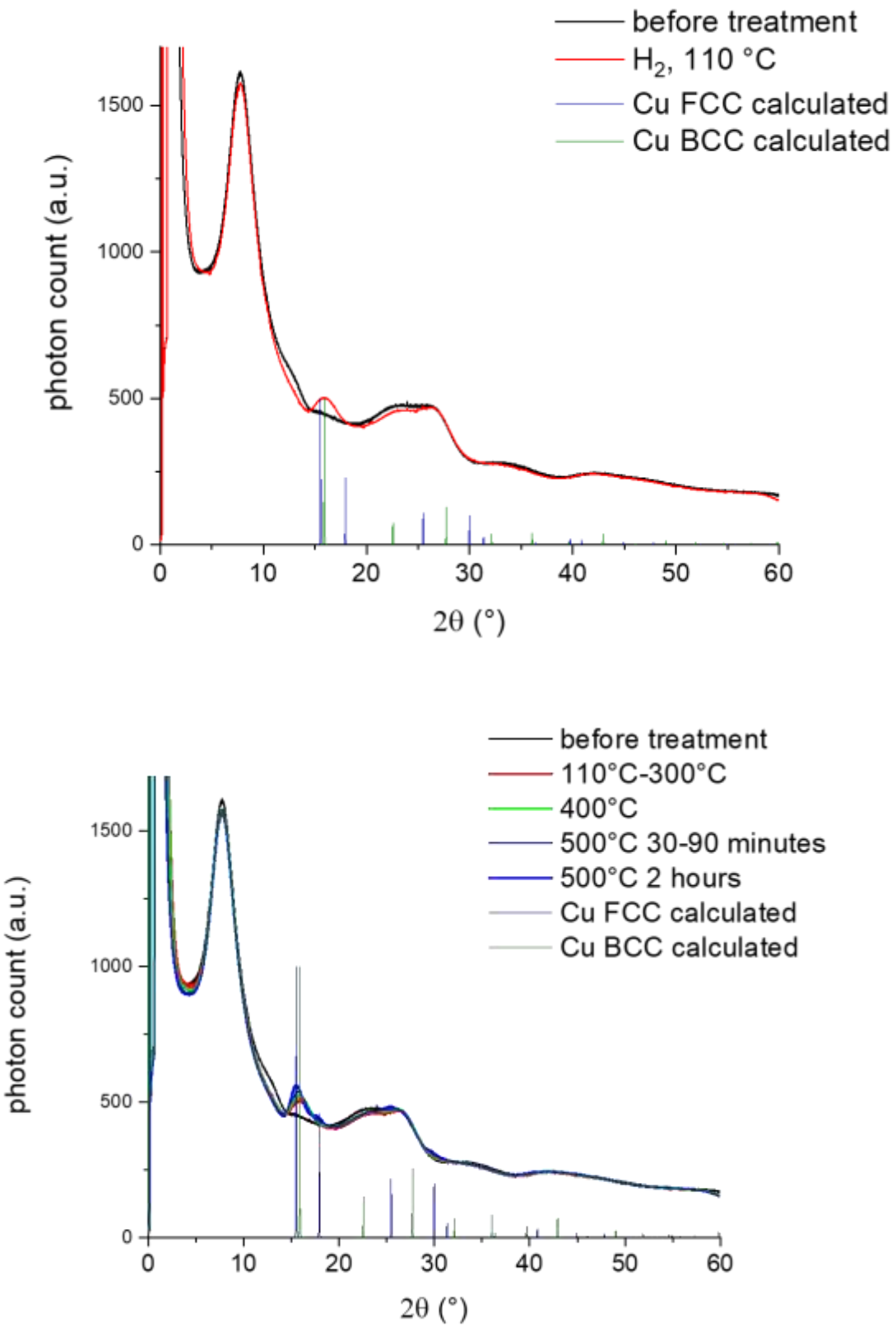

Figure S20: Entire data range measured during in situ H_2 reduction of ***[Cu']@SiO₂***

Debussy Simulation

Simulations were carried out using Debussy 2.0[9]. The models were nanocubes with an edge length of 2nm. The pair distance for FCC was d=2.556 Å, the pair distances for BCC d=2.556 Å and d=2.498 Å.

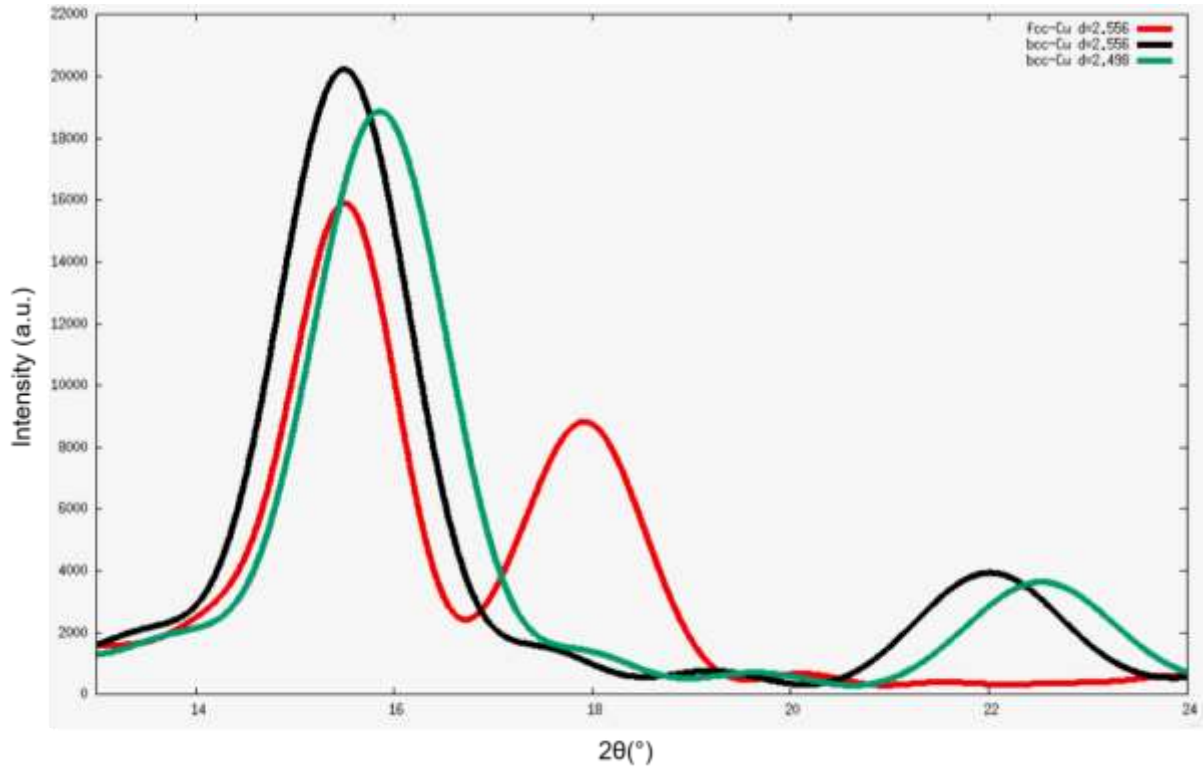

Figure S21: Simulation of the diffraction patterns for FCC and BCC structured Cu nanocubes with a diameter of 2nm.

Table ST3: Fit parameters for the DEBUSSY fits

T(°C)	Composition	a	d	wR	GoF
110	100% BCC	2.900	2.511	0.282%	1.91
500	88% BCC 12% FCC	2.945 3.639	2.551 2.573	0.469%	3.27

Debye-Scherrer Analysis

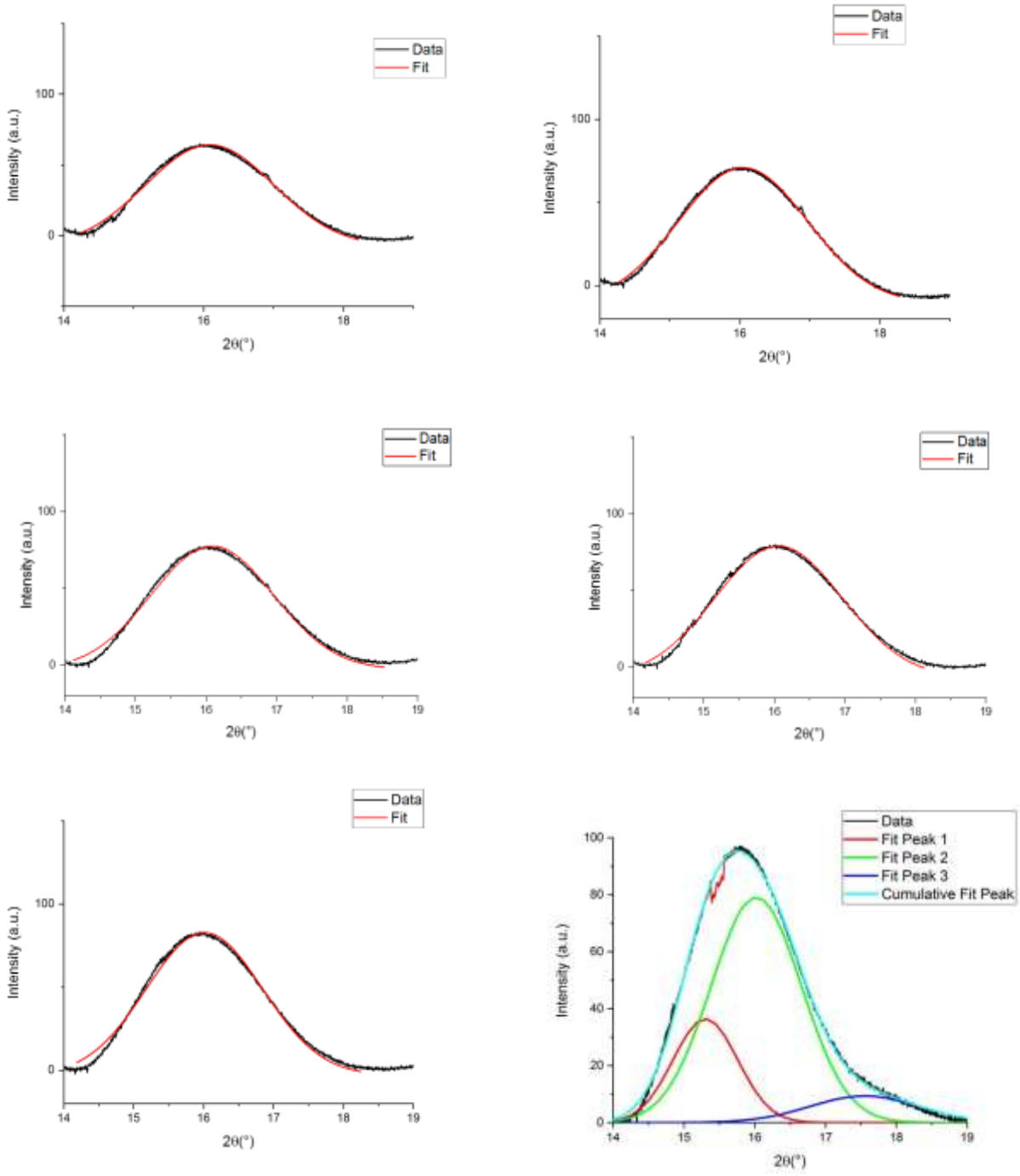

Figure S22: Gaussian Fits to the in situ pXRD Data at (from top left to bottom right) : 110°C, *150°C, 200*°C, 300, °C, 400°C and 500°C

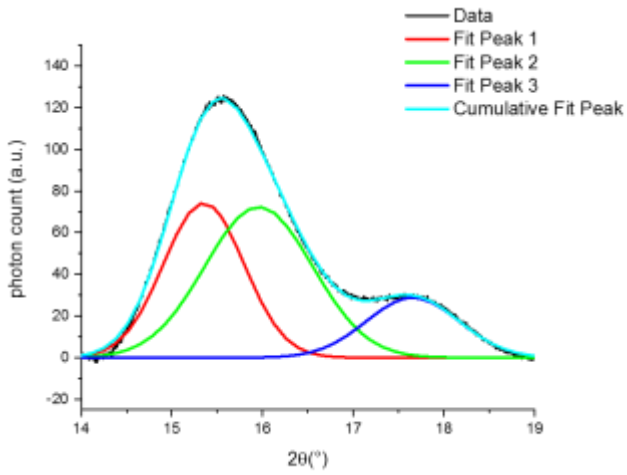

Figure S23: Gaussian Fit to the in situ pXRD data after 2 hours at 500°C

Table ST4: Fit parameters of Gaussian fits to in situ pXRD data. For the data points which require three peaks to fit, errors are too high to carry out Scherrer analysis. Due to high correlations between different fit parameters, peak positions were first determined by fitting and then fixed to estimate peak width.

T (°C)	2θ(°)	a (Å) and resulting Cu-Cu distance (Å)	β(°)	Estimated Crystallite size (nm)
110	16.085 ± 0.002	2.87 (2.49)	2.17 ± 0.01	1.34
150	16.043 ± 0.001	2.88 (2.49)	2.167 ± 0.006	1.36
200	16.088 ± 0.002	2.87 (2.49)	2.039 ± 0.009	1.45
300	16.060 ± 0.002	2.88 (2.49)	2.12 ± 0.01	1.40
400	16.010 ± 0.001	2.88 (2.49)	1.959 ± 0.009	1.51
500	15.3 16 17.6	3.70 (2.62) 2.89 (2.5)	1 ± 7 1 ± 5 1.8	
500 (2 hours)	15.4 16 17.6	3.68 (2.6) 2.89 (2.5)	1 ± 4 1 ± 5 1 ± 10	

5: Computational Details

General considerations:

All Calculations were performed using the Vienna *Ab initio* Simulation Package (VASP)[11-13] with a cut-off energy of 400 eV. The structures were optimized using the projector augmented wave (PAW) method (plane-wave basis set with pseudopotentials)[14,15] using the official VASP pseudopotentials[16] and the Perdew-Burke-Ernzerhof (PBE) exchange-correlation functional.[17,18]

Structural Parameters

Bulk Structures

The structure of FCC- and BCC-structured Cu was optimised. We first constructed the FCC- and BCC-unit cells based on the unit cell parameters of previously reported FCC- and BCC-Cu structures; for FCC-Cu, we used a = 3.60 Å as initial guess.[19] BCC-Cu proved to be more difficult, and we had to test multiple unit cell parameters until a stable bulk structure could be obtained for a = 2.89 Å as an initial guess.[20] We then optimized these unit cells and atomic positions by calculating the stress tensors and changing ionic positions, cell volume, and cell shape during the bulk optimisation (ISIF = 3).

The optimized unit cell parameters are a_{FCC} = 3.63 Å for FCC-Cu and a_{BCC} = 2.88 Å for BCC-Cu, which agrees well with previous published results for bulk FCC-Cu[19] and thin film of BCC-Cu on Fe.[20] The bulk structures are shown below; all structures were visualised using VESTA, a 3D visualisation program for structural models and 3D grid data such as electron/nuclear densities. [21]

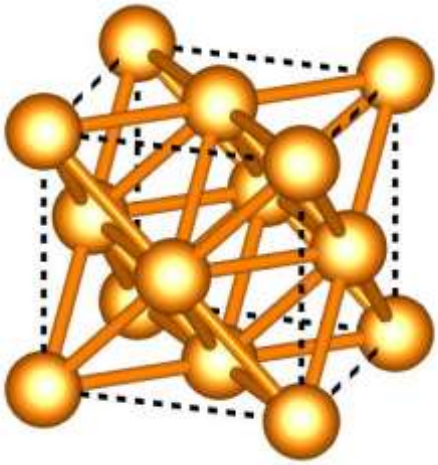

FCC-Cu

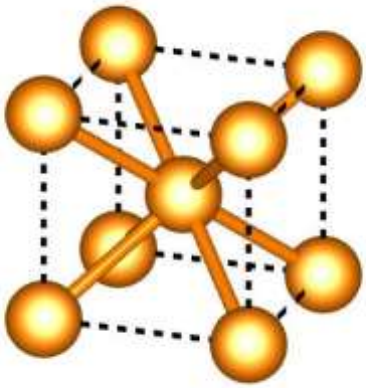

BCC-Cu

Slab Models

The used slab models are shown below:

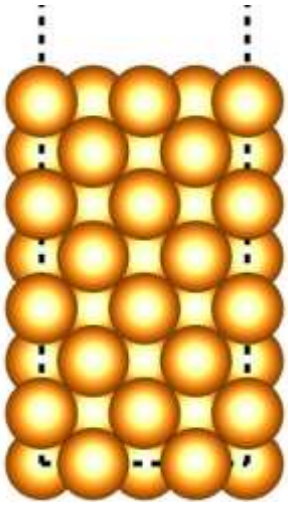

FCC-(100)

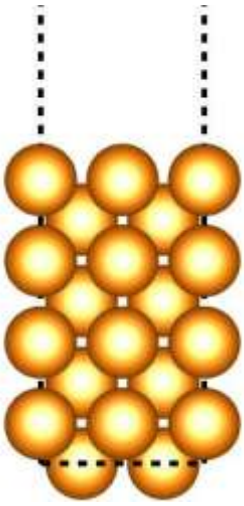

BCC-(100)

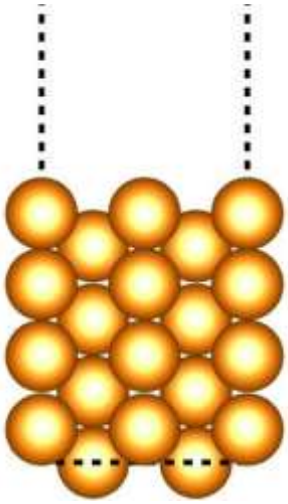

FCC-(110)

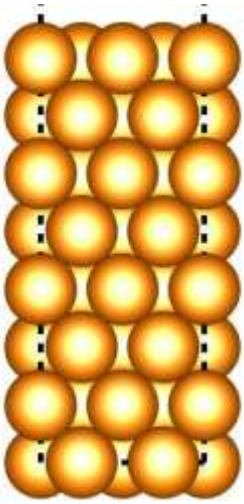

BCC-(110)

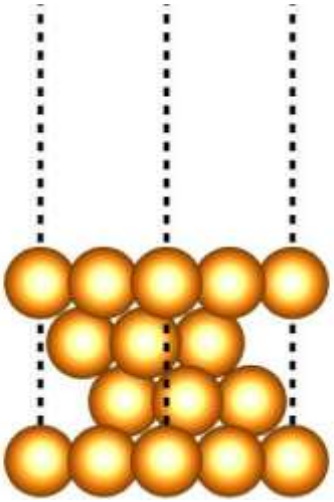

FCC-(111)

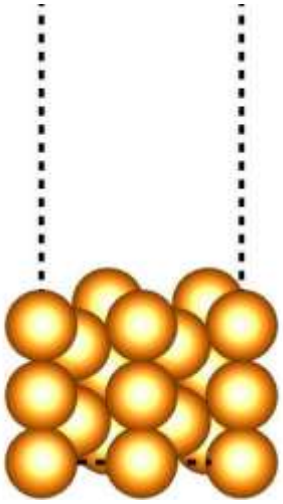

BCC-(111)

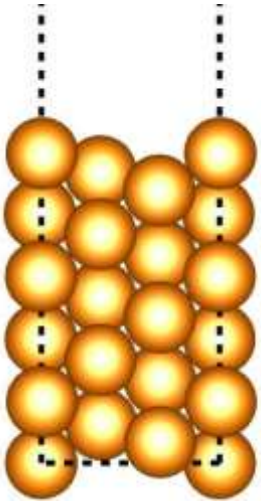

FCC-(211)

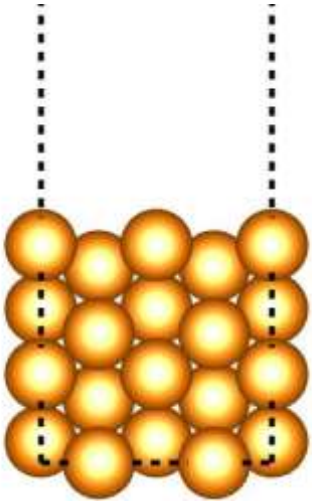

BCC-(211)

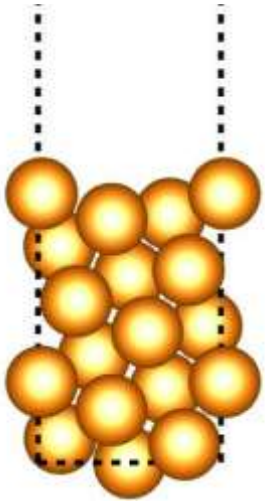

BCC-(210)

6. Ab initio Thermodynamics

The stability of all surfaces considering the adsorption at given conditions was calculated using *ab initio* thermodynamics[22]. We used the same approach as described in our last work[23].

Bulk Energy

The bulk energy of an atom in a crystalline solid is equal to its chemical potential, which is the contribution of that atom to the total bulk energy of an infinite crystal. Since the temperature-dependent terms for the total bulk energy of an infinite crystal are small as long as the temperature is much lower than the melting point of the crystal, these temperature-dependent terms can be safely neglected. Thus, it is reasonable to approximate the bulk energy at a specific temperature with the chemical potential of a substance at a temperature of 0 K and standard pressure ($\mu^{!}$), which is just the electronic energy of the substance as calculated by DFT-based calculations. Thus, for an atom X in a bulk structure with k atoms X in the unit cell, it is $k^{\#\$}$ part of the electronic energy of the unit cell (calculated by DFT):

$$\mu_{!}(T) \approx \mu^{!} = \frac{E_{!,!}}{k}$$

Chemical Potential of Gas Phase Species

For large enough temperatures and low enough pressures, the gas phase molecules can be approximated as an ideal gas. The chemical potential of an ideal gas Z can be written as sum of the chemical potential at a temperature of 0 K and standard pressure ($\mu^{"}$). The vibrational, rotational, and other temperature-dependent, but pressure-independent contributions $\Delta G_{\%}(T)$ can be calculated according to the following formula using the values in the thermochemical tables:

$$\Delta G_{\%}(T) = \Delta H_{\%}(T) - T \cdot \Delta S_{\%}(T) = H_{\%}(T) - H_{\%}(0\mathrm{K}) - T \cdot S_{\%}(T)$$

The pressure-dependent term is based on the ideal gas law and has the following form:

$$k_{\&} \cdot T \cdot \ln 5\frac{p_{\%}}{p^{"}}7$$

Combining these terms together gives the following equation describing the temperature- and pressure-dependency of the chemical potential of an atom in the gas phase:

$$\mu_{\%}(T) = \mu_{\%}^{"} + \Delta\mu_{\%} = \mu_{\%}^{"} + \Delta G_{\%}(T) + k_{\&} \cdot T \cdot \ln 5\frac{p_{\%}}{p^{"}}7$$

For a molecular gas such as dihydrogen (H_2), the chemical potential of a single atom is the atomic fraction of the molecular chemical potential. Thus, the chemical potential of H* in H_2 ($\mu_{'}$) is half the chemical potential of H_2 ($\mu_{'"}$).

$$\mu_{'}(T) = \frac{\mu_{'"}}{2} = \frac{1}{2} \cdot ;\mu_{'"}^{"} + \Delta G_{'"}(T) + k_{\&} \cdot T \cdot \ln 5\frac{p_{(}}{p^{"}}7<$$

For a fixed temperature ($T_)$), this expression can be simplified to the following equation depending linearly on the logarithm of the partial pressures of dihydrogen:

$$\mu_{*}(T) = a(T) + b(T) \cdot \ln\left(\frac{p_{H_2}}{p^{\ominus}}\right)$$

$$a(T) = \frac{\mu^{\ominus}_{H^*}(T) + \Delta G^{\ominus}_{ads}(T)}{2}; \quad b(T) = \frac{RT}{2}$$

where the chemical potential of H* in the gas phase for a fixed temperature depends only on the partial pressure of H_2.

Surface Energy

The surface energy γ is defined as the energy generated by a surface relative to the energy of an equivalent bulk structure, normalized by the surface area. For a surface of n_{bulk} atoms of bulk material X, the surface energy is defined as following using the bulk chemical potential:

$$\gamma_{*} = \frac{E_{surf} - n_{bulk} \cdot \mu^{\ominus}_{bulk}}{A}$$

If a hydrogen atom is adsorbed from the gas phase, the chemical potential of H* in the gas phase must be subtracted as well:

$$\gamma_{*,*H}(T) = \frac{E_{surf,*H} - n_{bulk} \cdot \mu^{\ominus}_{bulk} - n_{H} \cdot \mu_{H}(T)}{A}$$

The surface energy of a surface with adsorbed hydrogen atom thus depends on the bulk energy of the metal and the chemical potential of H* in the gas phase. Inserting the expression of the gas phase chemical potential in this expression results in the following expression linking the surface energy for a fixed temperature to the hydrogen partial pressure:

$$\gamma_{*,*H}(T, p_{H_2}) = \frac{1}{A} \cdot \left(c_{*,*H}(T) - n_H \cdot a(T) - n_H \cdot b(T) \cdot \ln\left(\frac{p_{H_2}}{p^{\ominus}}\right)\right)$$

$$c_{*,*H}(T) = E_{surf,*H} - n_{bulk} \cdot \mu^{\ominus}_{bulk} - \frac{n_H}{2}\left(\mu^{\ominus}_{H^*}(T) + \Delta G^{\ominus}_{ads}(T)\right)$$

The surface energy of any surface with different hydrogen coverage depends thus only on the hydrogen coverage (n_H) and the hydrogen partial pressure (p_{H_2}).

Surface Stability Diagrams In Hydrogen Atmosphere

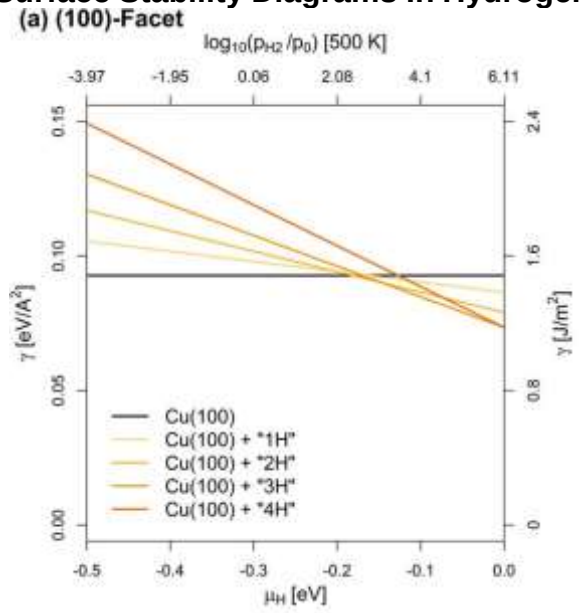

FCC-(100)

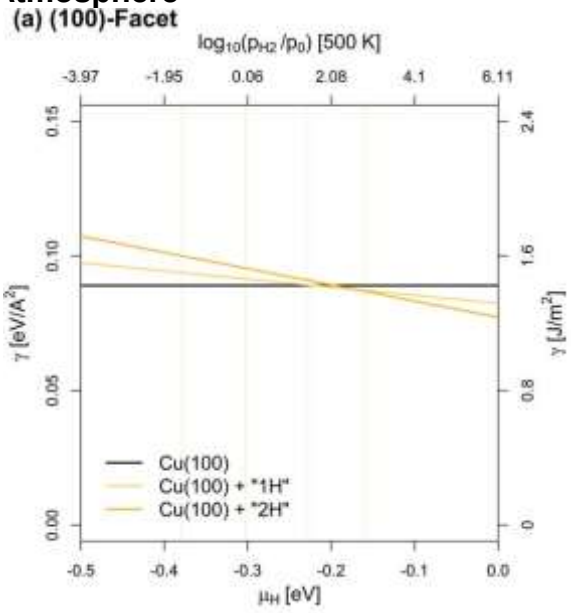

BCC-(100)

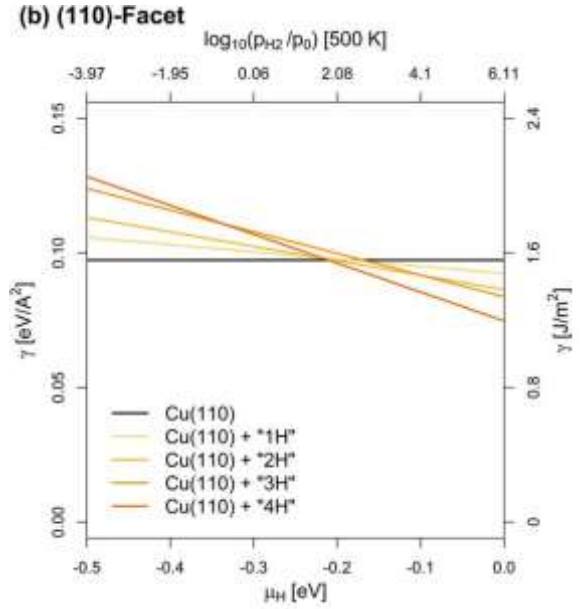

FCC-(110)

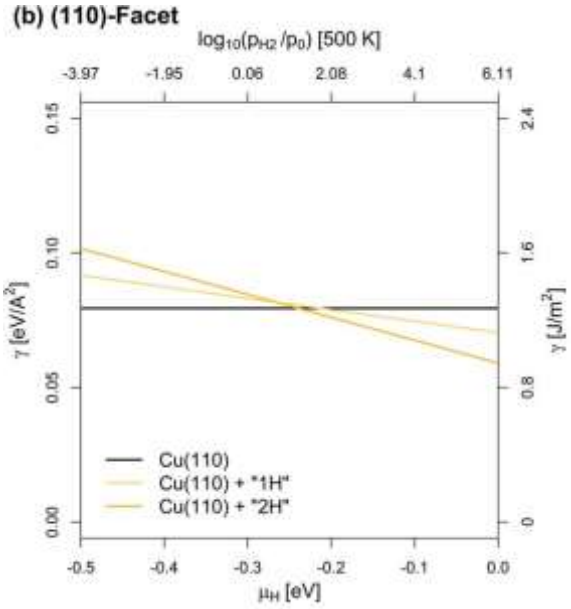

BCC-(110)

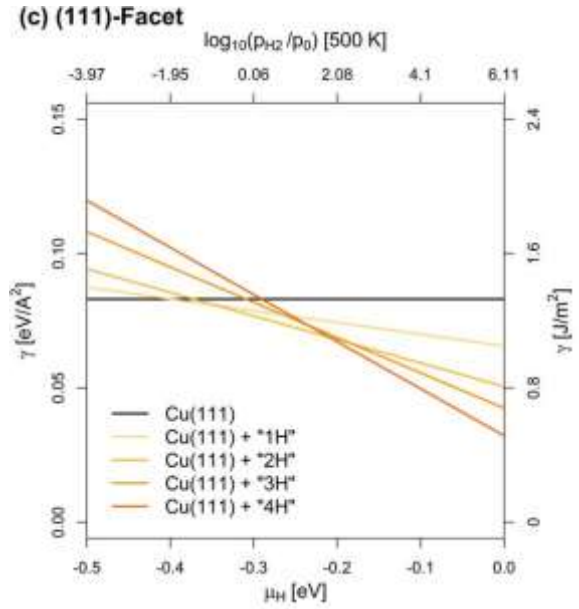

FCC-(111)

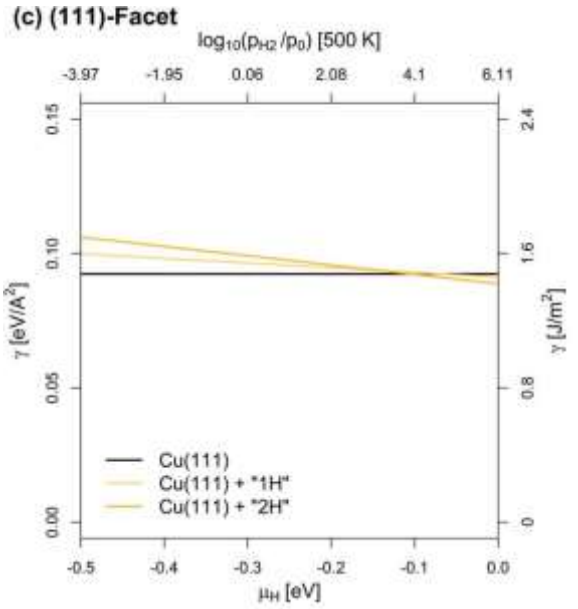

BCC-(111)

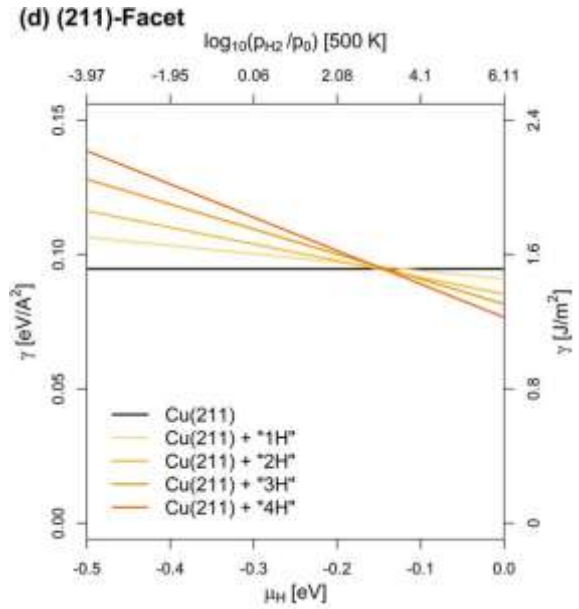

FCC-(211)

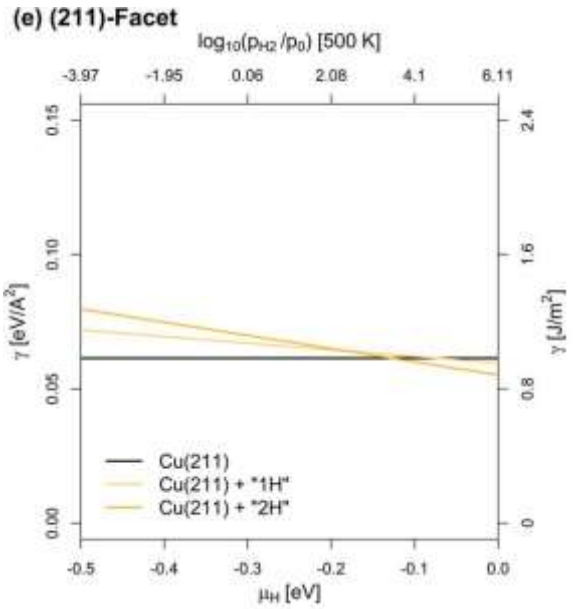

BCC-(211)

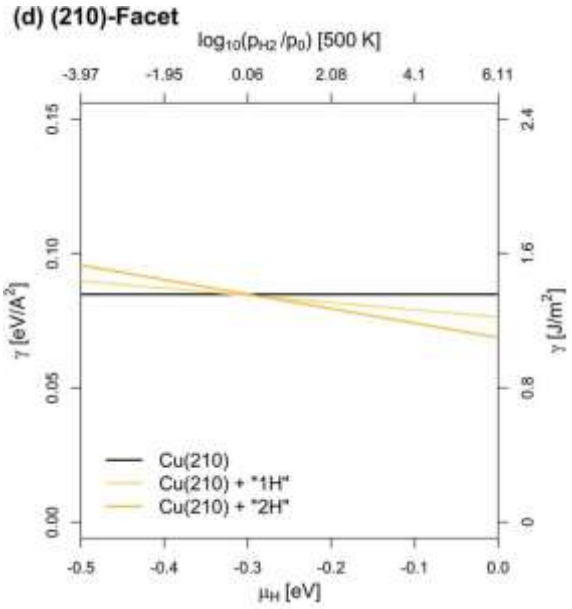

BCC-(210)

Surface Energy Depending on Hydrogen Chemical Potential

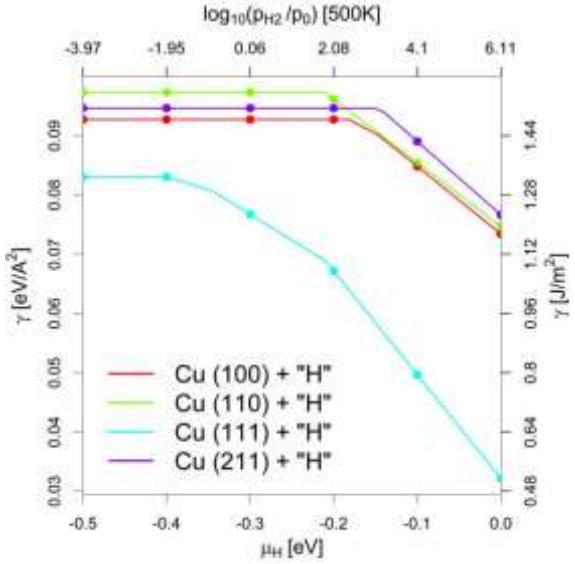

FCC-Cu

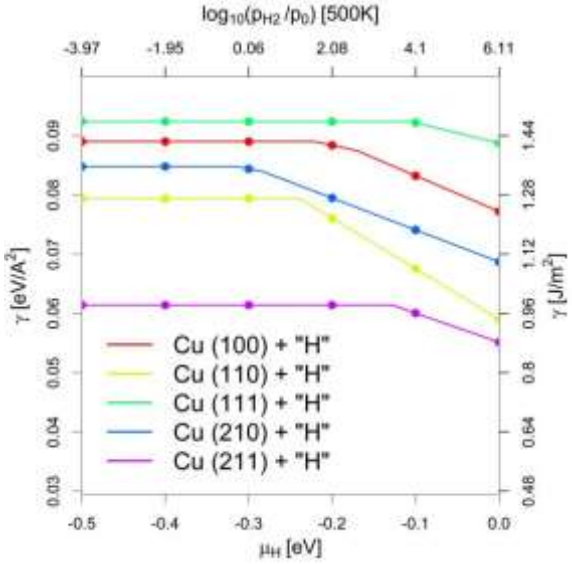

BCC-Cu

References

(1) A. Roussey, P. Gentile, D. Lafond, E. Martinez, V. Jousseaume, C. Thieuleux, C. Coperet, Cu nanoparticles on 2D and 3D silica substrates: controlled size and density, and critical size in catalytic silicon nanowire growth *J. Mat. Chem. C* **2013**, 1, 1583-1587.

(2) Sandoval, J. J.; Palma, P.; Álvarez, E.; Cámpora, J.; Rodríguez-Delgado, A. Mechanism of Alkyl Migration in Diorganomagnesium 2,6-Bis(Imino)Pyridine Complexes: Formation of Grignard-Type Complexes with Square-Planar Mg(II) Centers. *Organometallics* **2016**, *35* (18), 3197–3204.

(3) Meyer, E. M.; Gambarotta, S.; Floriani, C.; Chiesivilla, A.; Guastini, C., **1989**, Polynuclear Aryl Derivatives of Group 11 Metals: Synthesis, Solid State-Solution Structural Relationship, and Reactivity with Phosphines, *Organometallics*, 8, 1067-1079.

(4) Müller, O., Nachtegaal, M., Just, J., Lützenkirchen-Hecht, D., & Frahm, R. , **2016** Quick-EXAFS setup at the SuperXAS beamline for *in situ* X-ray absorption spectroscopy with 10ms time resolution. *J. Synchrotron Rad.*, *23*, 260-266

(5) Clark, A.H., Imbao, J., Frahm, R. and Nachtegaal, M. *ProQEXAFS*: a highly optimized parallelized rapid processing software for QEXAFS data, **2020**, *J. Synchrotron Rad*. 27, 551-557

(6) Ravel, B.; Newville, M. *ATHENA, ARTEMIS, HEPHAESTUS*: Data Analysis for X-Ray Absorption Spectroscopy Using *IFEFFIT*. *J. Synchrotron Radiat.* **2005**, *12* (4), 537–541.

(7) Windig, W. & Guilment, J. Interactive self-modeling mixture analysis. *Anal.Chem,* **1991**, 63, 1425–1432

(8) Bergamaschi, A.; Cervellino, A.; Dinapoli, R.; Gozzo, F.; Henrich, B.; Johnson, I.; Kraft, P.; Mozzanica, A.; Schmitt, B.; Shi, X. The MYTHEN Detector for X-Ray Powder Diffraction Experiments at the Swiss Light Source. J*. Synchrotron Radiat*. **2010**, *17*, 653−668

(9) A. Cervellino, R. Frison, F. Bertolotti and A. Guagliardi, DEBUSSY 2.0: the new release of a Debye user system for nanocrystalline and/or disordered materials, *J. Appl. Cryst.,* **2015**, 48, 2026

(10) Momma,K. and Izumi,F. VESTA: a three-dimensional visualization system for electronic and structural analysis, *J. Appl. Cryst., **2008**, 41,* 653-658

(11) G. Kresse and J. Hafner, Ab initio molecular dynamics for liquid metals

Phys. Rev. B, **1993**, *47*, 558

(12) G. Kresse, J. Furthmüller, Efficiency of ab-initio total energy calculations for metals and semiconductors using a plane-wave basis set, **1996**,*Computational Materials Science*, *6* (1), 15-50,

(13) G. Kresse, J. Furthmüller, Efficient iterative schemes for ab initio total-energy calculations using a plane-wave basis set, *Phys. Rev. B*, **1996**, *54*,

(14) P. E. Blöchl, Projector augmented-wave method

Phys. Rev. B , **1994**, *50*, 17953

(15) G. Kresse, D. Joubert, From ultrasoft pseudopotentials to the projector augmented-wave method, *Phys. Rev. B*, **1999**, *59*, 1758

(16) G Kresse, J Hafner, Norm-conserving and ultrasoft pseudopotentials for first-row and transition elements, *J. Phys.: Condens. Matter,* **1994**, *6*, 8245

(17) J. P. Perdew, K. Burke, M. Ernzerhof, Generalized Gradient Approximation Made Simple, *Phys. Rev. Lett*., **1996**, *77*, 3865

(18) J. Paier, R. Hirschl, M. Marsman, G. Kresse The Perdew–Burke–Ernzerhof exchange-correlation functional applied to the G2-1 test set using a plane-wave basis set, *J. Chem. Phys*. **2005**, *122*, 234102

(19) G. Brauer, *Handbuch der Präparativen Anorganischen Chemie*, Ferdinand Enke, Stuttgart, **1978**, vol. 3

(20) J. Z. Liu, A. van de Walle, G. Ghosh, and M. Asta, Structure, energetics, and mechanical stability of Fe-Cu bcc alloys from first-principles calculations, *Phys. Rev. B,* **2005**, *72,* 144109

(21) K. Momma and F. Izumi, VESTA 3 for three-dimensional visualization of crystal, volumetric and morphology data, *J. Appl. Crystallogr.*, **2011**, *44*, 1272-1276.

(22) K. Reuter, M. Scheffler,Composition, structure, and stability of RuO_2(110) as a function of oxygen pressure, *Phys. Rev. B,* **2001**, *65*, 035406